Earth and Planetary Science Letters 355–356 (2012) 162–173

Contents lists available at SciVerse ScienceDirect

Earth and Planetary Science Letters

journal homepage: www.elsevier.com/locate/epsl

Rates of magma differentiation and emplacement in a ballooning pluton recorded by U–Pb TIMS-TEA, Adamello batholith, Italy

Blair Schoene [a,b,*], Urs Schaltegger [b], Peter Brack [c], Christopher Latkoczy [d,1], Andreas Stracke [c,2], Detlef Günther [d]

[a] Princeton University, Department of Geosciences, Guyot Hall, Princeton, NJ 08544, USA
[b] University of Geneva, Section of Earth and Environmental Sciences, Geneva, Switzerland
[c] ETH Zurich, Department of Earth Sciences, 8092 Zürich, Switzerland
[d] ETH Zurich, D-CHAB, Lab of Inorg Chem, Wolfgang-Pauli-Str. 10, 8093 Zurich, Switzerland

ARTICLE INFO

Article history:
Received 4 November 2011
Received in revised form
8 August 2012
Accepted 16 August 2012
Editor: T. Elliot

Keywords:
U–Pb geochronology
ID-TIMS
plutonic systems
magmatic processes
zircon
titanite

ABSTRACT

Geochemical, structural, field, and geochronological data have been used to arrive at very different models for the construction of upper crustal batholiths. Models for pulsed intrusion of small magma batches over long timescales (>1 Ma) versus transfer of larger magma bodies on shorter timescales predict a different thermal, metamorphic, and rheological state of the crust, highlighting the importance of robust time constraints. This study focuses on a well-characterized upper crustal intrusion, the 15 km^2 Lago della Vacca complex (LVC), Adamello batholith, N. Italy. Previous studies used structural and petrologic data to argue that the LVC was emplaced through pulsed magma injection and in situ expansion (or, ballooning) of a short lived ($\sim 10^5$ yr) magma chamber. We test this model using a dense sampling strategy and high-precision ID-TIMS U–Pb geochronology of zircon and titanite combined with hafnium isotope and trace element analyses of the same volume of dated mineral (U–Pb TIMS-TEA). These data show that the marginal mafic pulses of magma crystallized zircon with primitive Hf isotopes and negligible Eu anomalies during fractional crystallization and ascent through the crust on 10–30 ka timescales. Subsequent, more felsic pulses yield individual zircon dates spanning as much as 200 ka within single handsamples and restrict the total construction time of the LVC to <300 ka. Rim to core solidification of the LVC, as recorded by titanite U–Pb thermochronology, occurred in ≥ 300 ka. U–Pb TIMS-TEA data from these complicated zircon populations limit the sources of antecrystic zircon, constrain AFC processes within host magmas, and illustrate the difficulty in interpreting zircon dates as magma emplacement ages. These data are supportive of growth of the LVC by a pulsed ballooning-type process over $\sim$300 ka, with the restriction that the rims of the LVC had solidified prior to the center-most injection, providing important constraints for thermomechanial models and strain analysis of the LVC and other balloon-like intrusions.

1. Introduction

Calibrating the timescales of magma generation, transport, and storage in the crust is important for building robust models for the thermal, rheological and geochemical evolution of the lithosphere (Annen, 2011; Annen et al., 2006; Laube and Springer, 1998; Sandiford et al., 2002). There is still considerable uncertainty, however, regarding the rates and mechanisms of magma flux into the middle and upper crust (Coleman et al., 2004; Glazner et al., 2004; Grunder et al., 2006; Matzel et al., 2006; Schaltegger et al., 2009). These parameters are essential for understanding the interaction between regional deformation and magma differentiation and also the methods by which space is made during emplacement (Brown, 2007; Glazner and Bartley, 2006; Hollister and Crawford, 1986; Hutton et al., 1990; Paterson and Vernon, 1995; Vigneresse, 1999).

U–Th–Pb and U-series geochronology have become invaluable tools for calibrating the tempo of eruptive and intrusive processes on <1 Ma to much longer timescales because the high closure temperature for diffusion of Pb in zircon suggests that dates record the time of crystal growth in magma (Bachmann et al.,

* Corresponding author. Princeton University, Department of Geosciences, 219 Guyot Hall, Princeton, NJ 08544, USA. Tel.: +1 609 258 5747; fax: +1 609 258 2593.
E-mail address: bschoene@princeton.edu (B. Schoene).
[1] Present address: Nanotion AG, Technoparkstrasse 1, 8005 Zurich, Switzerland.
[2] Present address: University of Münster, Institut für Mineralogie, Corrensstraße 24 D-48149 Münster, Germany.

0012-821X/$ - see front matter © 2012 Elsevier B.V. All rights reserved.
http://dx.doi.org/10.1016/j.epsl.2012.08.019

2010; Charlier and Wilson, 2010; Coleman et al., 2004; Crowley et al., 2007; Glazner et al., 2004; Lissenberg et al., 2009; Matzel et al., 2006; Reid and Coath, 2000; Schaltegger et al., 2009; Schmitt et al., 2010; Schoene and Bowring, 2010; Wilson and Charlier, 2009). Isotope dilution thermal ionization mass spectrometry (ID-TIMS) U–Pb dating, because of its high-precision relative to in situ dating techniques, has recently played a key role in rekindling discussion about the volumes and rates of magma emplacement (Glazner and Bartley, 2006; Glazner et al., 2004; Michel et al., 2008; Miller et al., 2007; Paterson et al., 2008). In particular, populations of zircons from single mappable intrusions have given weighted mean U–Pb zircon dates that differ by 10^5–10^6 yr over many km distance (Coleman et al., 2004; Glazner et al., 2004; Matzel et al., 2006; Memeti et al., 2010). These data have been used to suggest that large plutons are assembled over more than million-year timescales by the amalgamation of small pulses of magma, thus downplaying the importance of large magma chambers in generating batholiths. It is important that such models assume that a U–Pb zircon date records the timing of emplacement of magma, as opposed to pre-emplacement crystal growth, inheritance, etc. As a result of increased age precision beyond the 0.1% level in U–Pb ID-TIMS geochronology, it is becoming increasingly common to find populations of zircons on the hand sample scale that record crystal growth over 10^4–10^6 yr (Lissenberg et al., 2009; Schaltegger et al., 2009; Schoene et al., 2010a). On one hand, such data present difficulties because a zircon date does not necessarily represent the process of interest, for example the intrusion of magma. On the other hand, that such minerals record crystal growth despite prolonged exposure to magmatic temperatures implies these minerals contain a geochemical record of the liquids from which they crystallized (Belousova et al., 2002; Cavosie et al., 2004; Griffin et al., 2002; Hoskin and Schaltegger, 2003; Reid et al., 2010; Vazquez and Reid, 2002), which can therefore be used to constrain the geochemical evolution of magmatic systems in absolute time.

This study focuses on the Lago della Vacca complex (LVC), which forms a portion of the incrementally assembled ca. 40 Ma Re di Castello pluton, Adamello Batholith, Italy (Fig. 1; Schaltegger et al., 2009). Structural data, such as concentric, margin parallel magmatic fabrics and decreasing strain towards the intrusion center, have been used to model the LVC as a balloon-like intrusion that was emplaced by incremental magma pulses on $\sim 10^5$ yr timescales (Fig. 2; Brack, 1985; John and Blundy, 1993). The accuracy of such models is dependent on the combined timescales and lengthscales of magma intrusion because these determine the rheology of magma and host rock during emplacement and influence super- and subsolidus strain (e.g. Annen et al., 2006; Annen, 2011; Bateman, 1985; Ramsay, 1989; Cruden, 1990; John and Blundy, 1993; Paterson and Vernon, 1995). Here we present geochronological data on a balloon-like pluton, and test the ballooning model using a new method that combines U–Pb ID-TIMS zircon and titanite geochronology with trace element analysis (U–Pb TIMS-TEA; Schoene et al., 2010b). U–Pb dates are measured by ID-TIMS and geochemistry and Hf isotopes by inductively coupled plasma mass spectrometry (ICP-MS) on the remaining liquid (Schoene et al., 2010b). High-density sampling examines the LVC and our unique analytical approach also addresses questions more generally applicable to magmatic

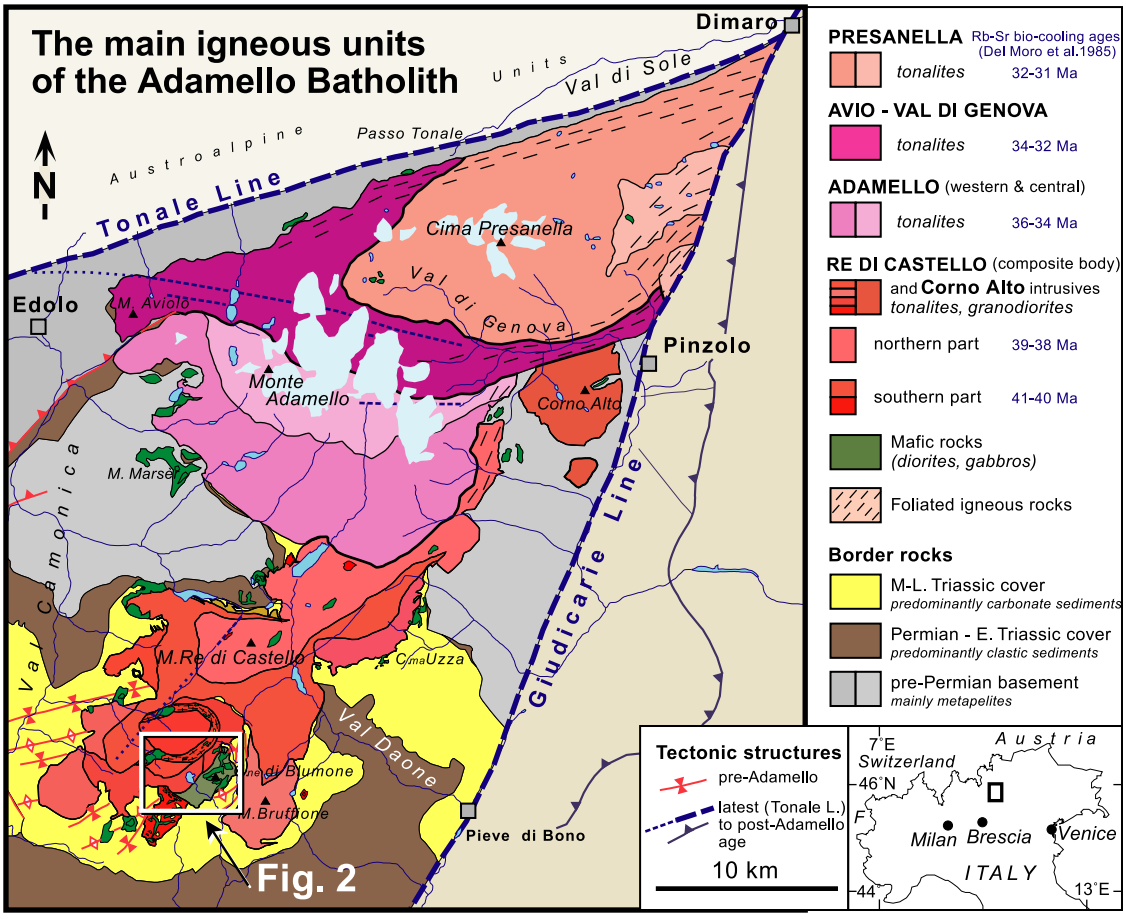

Fig. 1. Simplified geologic map of the Adamello batholith after Schaltegger et al. (2009), illustrating the approximate ages, lithologic characteristics, and designations of the main igneous units. See Schaltegger et al. (2009) for more detailed map and geochronology of the Re di Castello pluton. Location of the field site and Fig. 2 is outlined by the white box.

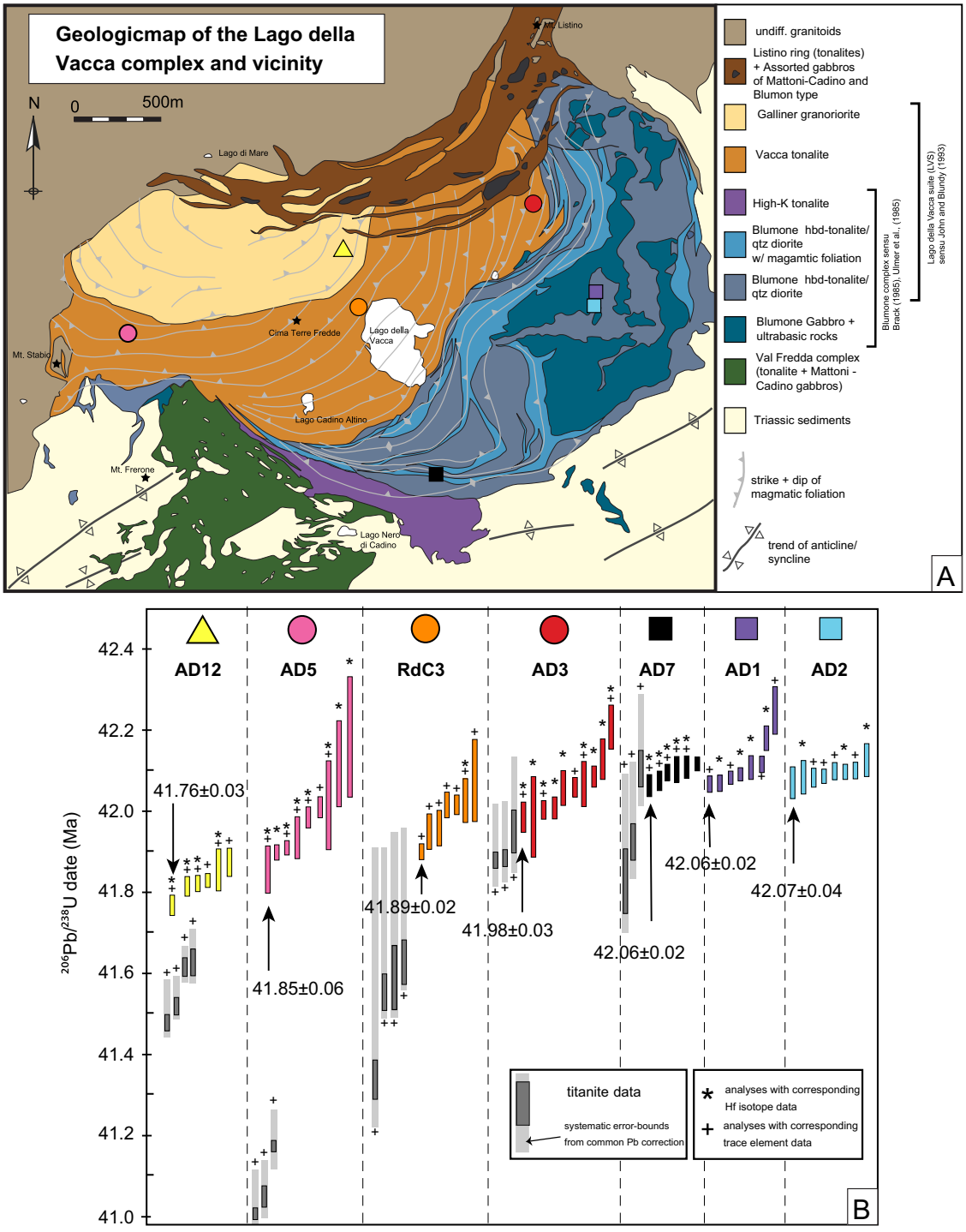

Fig. 2. (A) simplified geologic map of the study area after John and Blundy (1993). Sample locations indicated by symbols. (B) U–Pb geochronology showing $^{206}Pb/^{238}U$ dates for individual zircon and titanite. Each bar is an individual analysis and the size of vertical bars are $\pm$2-sigma. Crystallization age and uncertainty of youngest zircon from each sample is written out for reference. Colors match sample locations in (A) and samples also separated by vertical dashed lines. All titanite analyses are gray, but correspond to samples within the same vertical dashed lines. The systematic uncertainty in titanite dates arising from unknown common Pb composition produces a systematic error, estimated here by the light gray bars that represent changing the composition estimate by the Stacey and Kramers (1975) Pb evolution model between 0 and 200 Ma, from 42 Ma that was used to reduce data in dark gray (see text for more information).

systems: Which zircons from a hand sample, if any, date the final emplacement of the magma? How are fractional crystallization, assimilation and magma mixing recorded in accessory mineral geochemistry? What are the post-intrusion cooling rates, and can we quantify these? We show that these new types of data can help us better interpret high-precision dates and also lead to a richer understanding of the timescales and processes of pluton construction.

2. Geologic background

The Adamello batholith is an excellently exposed ca. 42–30 Ma alpine intrusion located in the Southern Alps of Northern Italy (Fig. 1; Brack, 1985; Del Moro et al., 1985b). Dramatic topography exposes >2 km vertical relief over $\sim$670 km^2. The Re di Castello pluton (RdC) in the south is the oldest portion of the batholith and centers around two ultramafic to gabbroic intrusive series,

the Val Fredda and Blumone complexes. Ulmer et al. (1985) and Kagami et al. (1991) interpreted these mafic intrusions as mantle melts that subsequently differentiated via fractional crystallization in the middle to lower crust to arrive at gabbroic to dioritic compositions. Kagami et al. (1991) used Nd and Sr isotopic data from the RdC to show that the tonalitic to granodioritic compositions resulted from continued fractionation in addition to crustal assimilation. A subset of these km-sized fine-grained varieties of tonalite and granodiorite intruded ca. 42.5 – 41.0 Ma as discrete magma pulses with zircon Hf isotope compositions that show decreasing amounts of crustal assimilation within this window (Schaltegger et al., 2009). Sr and oxygen isotopic evidence, however, shows an increasing amount of crustal assimilation over ~10 Ma from south to northeast across the entire Adamello batholith (Cortecci et al., 1979; Del Moro et al., 1985a).

Brack (1985) argued that the RdC intruded by a combination of "passive" processes involving stoping and block rotation to more "forceful" intrusive processes that deformed the surrounding host rocks. Examples of passive intrusion were observed by Brack (1985) in the margins of the RdC, while forceful intrusions are typified by the Vacca tonalite, which forms the centerpiece of our study. The Vacca tonalite and bordering units combined show a range in composition from ultramafic to granodioritic and include the Blumone complex and the Galliner granodiorite (Fig. 2). Several subsidiary units have been grouped both with the Vacca tonalite and the Blumone complex (see alternate groupings in Fig. 2). For the sake of simplicity, we group all rocks in the study area into the Lago della Vacca complex (LVC), including the Blumone complex, the Vacca tonalite and the Galliner granodiorite.

John and Blundy (1993) proposed a model in which early emplacement of the LVC (e.g. the Blumone gabbro) involved brittle fracture and stoping of country rocks (see also Brack, 1985). Margin-parallel magmatic foliations and increasing magmatic strain towards the margins of the LVC indicated a transition towards incremental forceful intrusion of inner magma pulses. This model is not unlike ballooning models in other systems (e.g. Paterson and Vernon, 1995), though John and Blundy (1993) pointed out that measured strain integrated along the margins of the intrusion cannot alone account for the volume of material emplaced in the interior. They thus proposed that contraction of the marginal units during solidification can provide some space for subsequent pulses. Further analysis by John and Stünitz (1997) discussed the importance of late stage melt segregation and deformation in the margins of the LVC. Brack (1985) noted the apparent dextral offset in anticline–syncline pairs within Mesozoic sedimentary units (these folds are depicted in Fig. 2) as evidence for the eastward translation of the Blumone complex due to forceful intrusion of the Vacca tonalite. An approximate duration for the intrusion was calculated by John and Blundy (1993), who use a simple thermal model to show that a single magma chamber the size and composition of the Lago della Vacca complex would completely solidify in <60 ka without the input of extra heat.

3. Samples and results

Seven samples of the Lago della Vacca complex (LVC) were collected for U–Pb TIMS-TEA. Sample locations are given in Fig. 2, and more detailed sample and zircon descriptions are given in the Supplementary material. Hand sample and field photos are shown in Supplementary material Fig. S1, zircon cathodoluminescence images are in Supplementary material Fig. S2. Two samples from pegmatitic segregations of the Blumone gabbro (AD1, AD2) were collected. Sample AD7 is a hornblende-rich quartz diorite that comes from what John and Blundy (1993) term the low-K marginal unit of the Vacca tonalite. Three samples (AD3, AD5, and RdC3) come from the Vacca tonalite. These are hornblende biotite tonalites that are indistinguishable in hand sample and thin section, though AD5 has minor potassium feldspar. The Galliner granodiorite (AD12) is distinguished from the Vacca tonalite by coarser biotite phenocrysts and a less-pronounced magmatic fabric.

U–Pb ID-TIMS geochronology was carried out on the same dissolved minerals as trace element and Hf isotope measurements. Methodology and data tables for U–Pb ID-TIMS analyses, solution multicollector ICP-MS Hf isotope data, and zircon and titanite solution ICP-MS trace element analyses are given in Supplementary material. All uncertainties in the text, data tables and figures are at the 2-sigma or 95% confidence level. U–Pb uncertainties include internal errors only for the purposes of this study, but should be augmented with tracer calibration and decay constant uncertainties if compared to data determined using other tracers or dating techniques (e.g. Schoene et al., 2006).

3.1. ID-TIMS U–Pb geochronology and Hf isotopes

U–Pb isotope data are located in Supplementary material Table S1 and hafnium isotopes in Supplementary material Table S2. Fig. 2 indicates which U–Pb analyses also have corresponding Hf isotopic and TEA data. Sixteen zircons were analyzed from gabbroic AD1 and AD2, and these analyses cluster around a $^{206}Pb/^{238}U$ date of 42.08 Ma with uncertainties on single zircons of 0.02–0.06 Ma (Fig. 2). Two analyses from AD1 are distinctly older yielding a weighted mean on 8 with an MSWD of 11.3. All eight analyses from AD2 yield statistically equivalent $^{206}Pb/^{238}U$ dates with a weighted mean of 42.09 ± 0.01 Ma (MSWD = 1.0), indicating these zircons crystallized quickly (~20–40 ka). Six of seven zircons analyzed for Hf isotopes show a relatively restricted range of epsilon hafnium at the time of crystallization ($\varepsilon_{Hf(T)}$) of 4.7–6.6 (Supplementary material Table S2).

Six zircons from quartz diorite sample AD7 were analyzed and these give $^{206}Pb/^{238}U$ dates that range between 42.06 and 42.11 Ma (± 0.02 Ma on single grains; Fig. 2). A weighted mean yields an MSWD of 3.1, indicating these zircons crystallized over a resolvable period of time of at least 50 ka. Five of six dated zircons yielded $\varepsilon_{Hf(T)}$ from 10.0 to 11.4. Three titanite analyses, each consisting of two subhedral grains, gave $^{206}Pb/^{238}U$ dates between 41.83 and 42.10 Ma.

Between 8 and 11 zircons were analyzed from each of the three Vacca tonalite samples (AD3, RdC3 and AD5). Each sample yielded a population of zircons with $^{206}Pb/^{238}U$ dates spanning between 200 and 400 ka (ca. 42.2–41.8 Ma), and one zircon from each sample is distinctly older (42.90, 43.65, and 60.40 Ma, with individual uncertainties from 0.01 to 0.10 Ma). The $\varepsilon_{Hf(T)}$ values fall between -0.4 and 3.1 with two higher values <7.5. Sample AD5 shows a trend in $\varepsilon_{Hf(T)}$ with time, increasing between -0.4 and 3.0 between ca. 42.2 and 41.8 Ma ($r^2 = 0.55$; Fig. 3A). Titanite from each sample was measured, and the age gap between the youngest zircon and the titanite dates increases from east to west across the Vacca tonalite. Sample AD3 (east) yields titanite dates that are 0–150 ka younger than the youngest zircon date, sample RdC3 (central Vacca) shows an ~300 ka gap, and sample AD5 (west) shows a difference of ~600–800 ka between the youngest zircon and the titanite dates.

Seven zircons were measured from the Galliner granodiorite (AD12; Fig. 2). One grain is 52.41 Ma, though the rest yield $^{206}Pb/^{238}U$ dates between 41.87 and 41.76 Ma (± 0.01–0.03 Ma on each grain). Hf isotopes show a decreasing $\varepsilon_{Hf(T)}$ trend from 4.3 to 2.6 over 120 ka ($r^2 = 0.85$; Fig. 3A). Titanite $^{206}Pb/^{238}U$ dates range from 41.62 to 41.52 (± 0.03 Ma) – 200–300 ka younger than the zircon dates.

Given the sensitivity of titanite dates to the common Pb correction (see analytical details in Supplementary material),

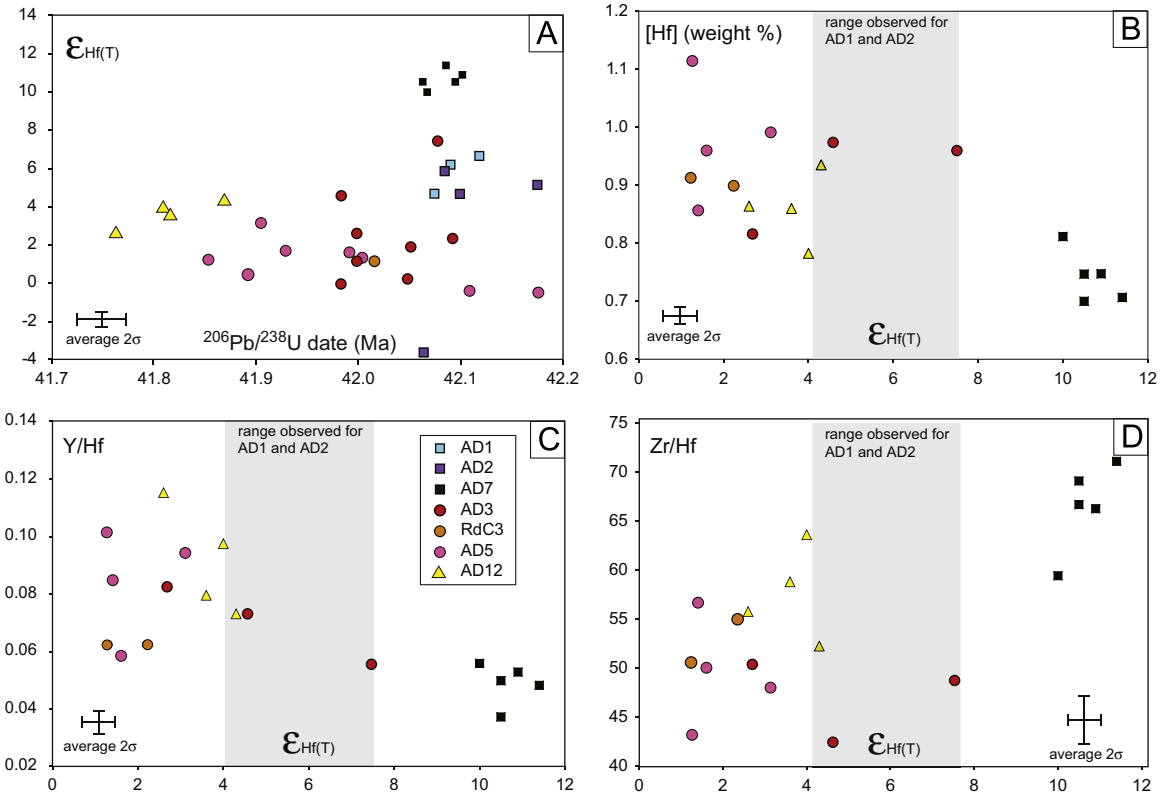

Fig. 3. Epsilon Hf, U–Pb date, and trace element data from single zircons. Average 2-sigma uncertainties are shown for each plot. Hf isotopes and trace element data from AD1 and AD2 were not successfully measured from the same grains, so the range of epsilon Hf is shown as a vertical gray bar in B–D (with one outlier removed). See Fig. 2 for sample locations and Supplementary material Tables S1–S3 for data.

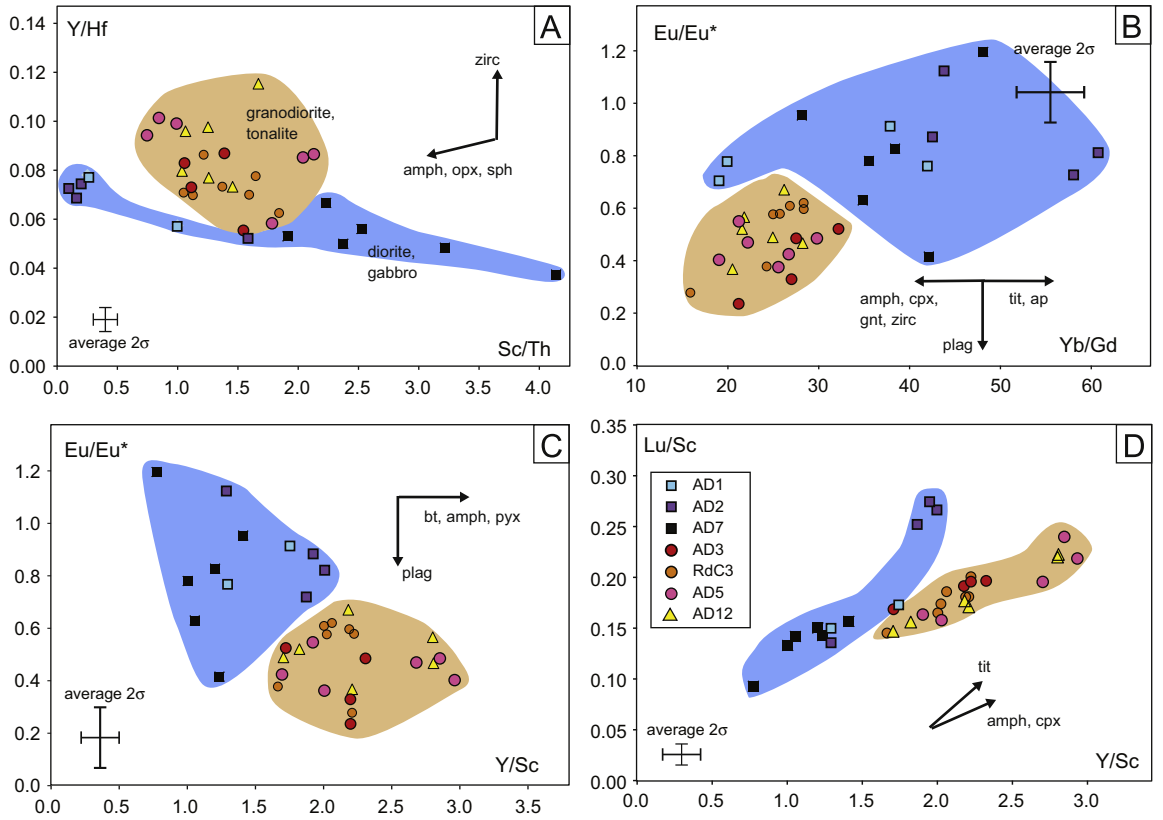

Fig. 4. Trace element correlation diagrams for zircons from the Lago della Vacca complex. Each data point represents a single zircon for which U–Pb isotopic were also obtained by ID-TIMS. The blue field encapsulates zircon from gabbroic to dioritic lithologies; the pink field contains zircons from tonalitic to granodioritic lithologies. See Fig. 2 for sample locations and Supplementary material Tables S1 and S3 for data. Average 2-sigma uncertainties are shown. Arrows indicate the approximate predicted direction zircon geochemistry would migrate given fractional crystallization of the indicated phases, assuming equilibrium partitioning between zircon and melt. Partition coefficients used are from Adam and Green (2006) and Bédard (2006). Abbreviations: plag=plagioclase, bt=biotite, amph=amphibole, pyx=pyroxene, opx=orthopyroxene, cpx=clinopyroxene, tit=titanite, zirc=zircon, gnt=garnet, ap=apatite. (For interpretation of the references to color in this figure caption, the reader is referred to the web version of this article.)

Fig. 2 plots the expanded uncertainty in the absolute dates by varying the Stacey and Kramers (1975) model Pb correction between 0 and 200 Ma, though 42 Ma was used to calculate dates. This uncertainty is systematic from sample to sample (it shifts points by the same amount within a sample), so trends between geochemistry and date discussed below are robust regardless of the choice in common Pb composition. See Supplementary material for additional discussion.

3.2. Trace element analyses (TEA) of ion exchange washes

Both Hf isotopes and trace elements were successfully measured from a subset of the same zircon aliquots measured for U–Pb isotopes (Tables S2 and S3; Fig. 3). The most primitive Hf isotopes are found in the diorite AD7 ($\varepsilon_{Hf(T)}$ 10–11), which correlate with low [Hf] (0.7–0.8% by weight) whereas the tonalitic (AD3, AD5, and RdC3) and granodioritic (AD12) samples have lower $\varepsilon_{Hf(T)}$ (average of ~3) and higher [Hf] (0.8–1.1%; Fig. 3B). High Y/Hf and low Zr/Hf also correlate with lower $\varepsilon_{Hf(T)}$ (Fig. 3C, D). No zircons from gabbroic samples AD1 or AD2 were successfully analyzed for both hafnium isotopes and trace elements; the range of observed $\varepsilon_{Hf(T)}$ from these samples is also shown in Fig. 3.

Trace element correlation diagrams show that zircon from different rocks types (e.g. gabbroic versus tonalitic) have distinct geochemical signatures and pronounced positive or negative trends that distinguish felsic from mafic rocks (Fig. 4). Compared to more mafic lithologies (gabbros AD1 and AD2 and diorite AD7), the Vacca tonalite (AD3, AD5, and RdC3) and Galliner granodiorite (AD12) have more pronounced negative Eu anomalies (Eu/Eu* < 0.7, Fig. 4B, C) and shallower HREE slopes (lower Yb/Gd; Fig. 4B).

U–Pb dates can be compared directly to trace element signatures of zircon and titanite. Zircon from the Vacca tonalite (samples AD3, AD5, and RdC3) show protracted crystallization over ~200 ka, and have trace element characteristics that are different in nearly every respect from the Blumone units (AD1, AD2, and AD7; Fig. 5). Certain trace element ratios from the three Vacca tonalite samples show weak correlations with time. For example, Y/Hf and Y/Sc increase over the period of 250 ka (r^2=0.10 and 0.26, respectively; Fig. 5A). Similarly, the Eu anomaly becomes less negative through the entire Vacca tonalite suite (r^2=0.14; Fig. 5B). Zircons from single samples have higher degrees of correlation, for example decreasing Eu/Eu* for RdC3 (r^2=0.47; Fig. 5B), increasing $\varepsilon_{Hf(T)}$ for AD5 (r^2=0.55; Fig. 3A), and decreasing Zr/Hf for AD5 (r^2=0.60; Fig. 5C). Zircon dates from the Galliner granodiorite span about 120 ka, and show trends in time with trace element ratios and Hf isotopes, such as decreasing $\varepsilon_{Hf(T)}$ (r^2=0.85; Fig. 3A), increasing Y/Hf (r^2=0.81; Fig. 5A).

Trace elements for titanite were also measured by TIMS-TEA for all samples except AD1 and AD2 (Fig. 6). Titanite from samples AD7 and AD3, whose dates overlap with the youngest zircon date from each sample, have invariant trace element signatures. RdC3 titanite also have relatively homogeneous trace element patterns, though are >200 ka younger than the youngest zircons from that sample. Titanite from samples AD5, AD7 and AD12 have highly variable trace element patterns and dates, and show correlations between U–Pb date and trace elements, which will be discussed below.

4. Discussion

4.1. Zircon as a recorder of magma chemistry

Despite evidence that non-equilibrium partitioning can have an effect on zircon trace element patterns at the sub-micron

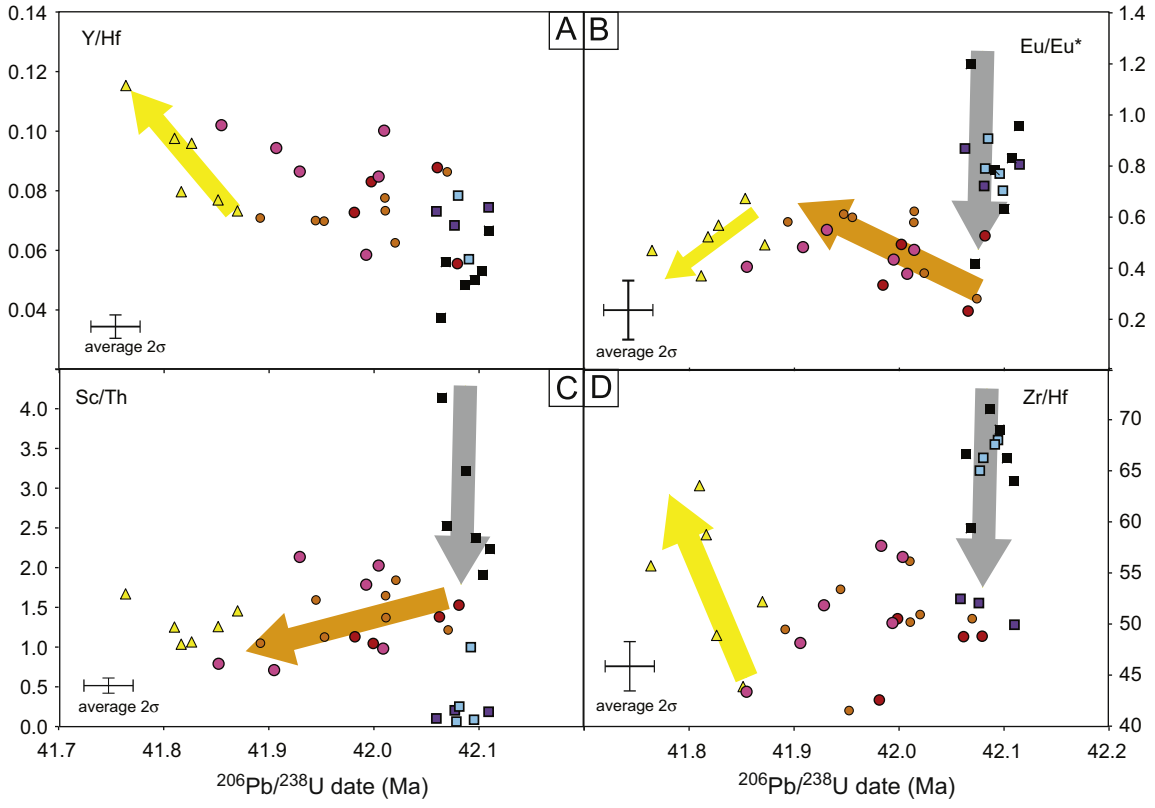

Fig. 5. Zircon trace elements with time determined by U–Pb TIMS-TEA. See Fig. 2 for sample locations and Supplementary material Tables S1 and S3 for data. Average 2-sigma uncertainties are shown for each plot. Arrows indicate inferred geochemical evolution of zircons from single hand sample with time, color-coded to sample color. See text for discussion. (For interpretation of the references to color in this figure caption, the reader is referred to the web version of this article.)

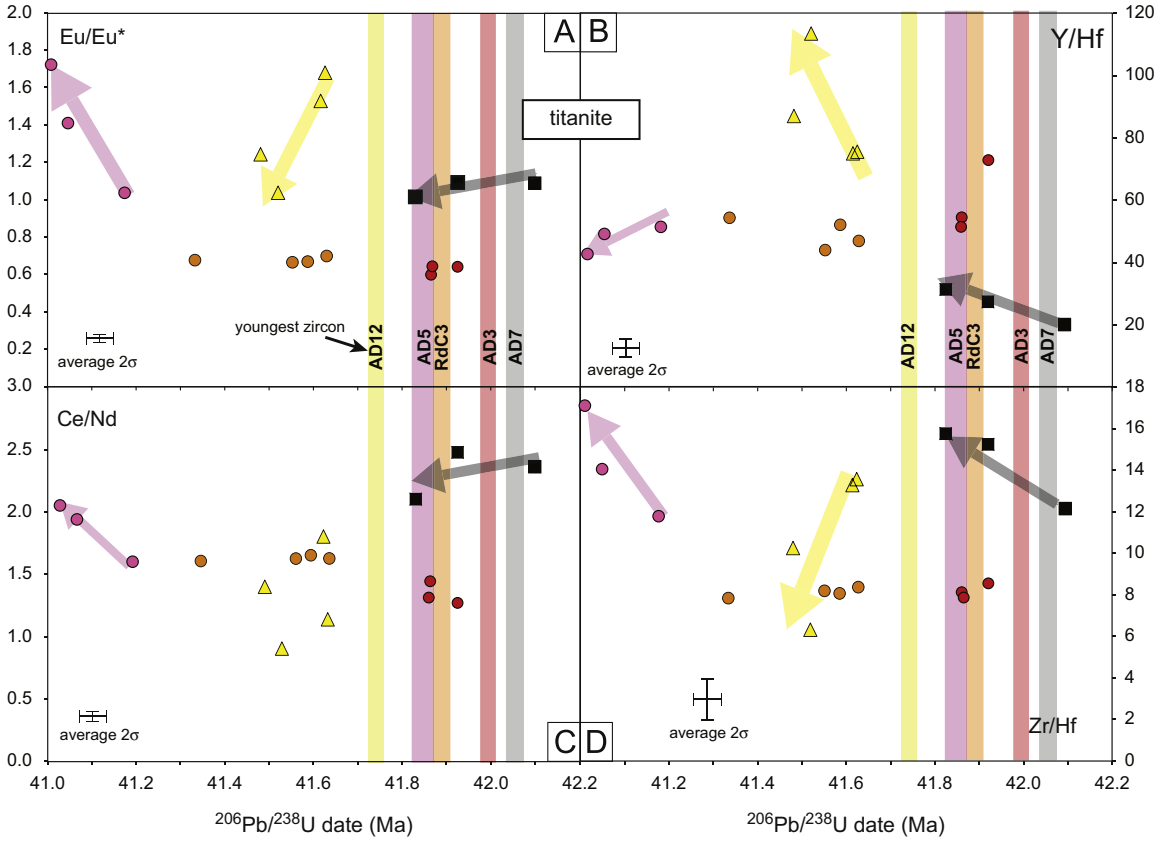

Fig. 6. Titanite trace elements with time determined by U–Pb TIMS-TEA. Symbols are the same as in Fig. 2; average 2-sigma uncertainties are shown for each plot. Vertical bars are color-coded dates of youngest zircon from each sample. Colored arrows highlight geochemical trends with time, requiring that some or all titanite from these samples grew subsolidus (see text for discussion). (For interpretation of the references to color in this figure caption, the reader is referred to the web version of this article.)

scale (Hofmann et al., 2009), numerous studies argue that zircon geochemistry reflects equilibrium partitioning between zircon and liquid (Barth and Wooden, 2010; Belousova et al., 2006; Claiborne et al., 2010, 2006; Reid et al., 2010; Schoene et al., 2010b). Important controls on equilibrium partitioning are temperature and magma composition, which have been explored in detail in other mineral-liquid systems, including titanite (Prowatke and Klemme, 2005, 2006a). Limited experimental partitioning data for zircon over a range of major element liquid compositions (e.g. variable SiO_2) and temperature show that zircon/melt partition coefficients decrease with higher temperature (Rubatto and Hermann, 2007). One may then expect that zircons from our mafic samples (AD7, AD1, and AD2) should have lower trace element concentrations than lower-temperature felsic samples (AD3, AD5, AD12, and RdC3). This is observed for samples AD7 and AD2 (e.g. [Hf], Fig. 3B), though zircon Hf isotopes clearly indicate these magmas are not cogenetic, weakening this comparison. Importantly, as discussed in Schoene et al. (2010b), whereas zircon/melt partition coefficients may vary by an order of magnitude over several hundred degrees (Rubatto and Hermann, 2007) and between empirical studies (Hanchar and van Westrenen, 2007; Sano et al., 2002; Thomas et al., 2002), the *ratios* of trace element partition coefficients are less strongly affected and also more consistent between studies. Therefore, we hypothesize that the observed differences in zircon trace element ratios (Figs. 4 and 5) record differences in magma chemistry, and explore the implications of this below in conjunction with zircon age and Hf isotopes.

4.2. Using U–Pb TIMS-TEA to document antecrystic zircon and magma evolution

Prolonged growth of zircon in magmatic systems provides an opportunity to constrain magma chemistry as a function of time and requires that we revisit the assumption that zircon dates record the intrusion of a pluton. Miller et al. (2007), following Bacon and Lowenstern (2005), Charlier et al. (2005), and others, discussed the terms autocryst, antecryst and xenocryst in the context of zircon geochronology and we use the terms similarly here. An autocryst is considered as a zircon that crystallized very late in the magmatic history of a hand sample at or very near the relative emplacement and sampling location. Antecrystic zircons are those that were inherited into a magma but that broadly originated in the same magmatic system (for example were transported from depth to the level of emplacement). Antecrystic zircons can therefore predate solidification of a magma by zero to millions of years. Xenocryst is used to reflect zircons that are inherited from fully crystallized country rock. Out of 58 zircons analyzed by ID-TIMS for this study, four can be argued to be xenocrystic based solely on age, ranging from 43.6 to 60 Ma, in that they predate any known magmatic activity in the Adamello.

U–Pb TIMS-TEA can provide a means of tracking the origins of zircon within a magmatic system if zircon chemistry can fingerprint the magma it grew in. To explore this, we examine the chemistry of zircons from magmas of different bulk composition. Whole–rock major and trace element compositions for the LVC are published in Ulmer et al. (1985), Kagami et al., (1991), and John and Blundy (1993). Fig. 3B–D shows that both $\varepsilon_{Hf(T)}$ and

various trace element ratios differ between zircons extracted from gabbroic to dioritic ("mafic"; AD1, AD2, AD7) versus tonalitic to granodioritic ("felsic"; AD3, AD5, RdC3, AD12) compositions. Given the ubiquitous presence of resorbed cores in zircon from all of the felsic samples (Supplementary material Fig. S2), it is possible that the roughly linear trends in Fig. 3B–D are created by mixing of antecrystic cores from mafic zircon such as AD7 with rims formed in a more felsic melt. Trends in trace element ratios through time (Fig. 5) do not support this scenario. Y/Hf (Fig. 5A) in zircons through time do fall on a linear trend with granodioritic zircons (AD12) on one end of the line and mafic zircons (AD7, AD1, AD2), on the other, older end of the line—consistent with mixing older chemically distinct antecrystic cores with younger rims. Other trace element ratios through time (Figs. 5B–D), however, do not show such a linear trend as would be expected by mixing cores and rims of endmember compositions and ages. Most importantly, in trace element correlation diagrams (Fig. 4), felsic and mafic zircons plot in entirely different fields with no overlap (the highlighted orange and blue fields in Fig. 4). An extremely fortuitous proportion of mafic core zircon and felsic rim zircon would be required in every single case to prevent overlap of these fields for example in Eu/Eu* versus Yb/Gd space (Fig. 4B).

These observations show that any transfer of zircon from mafic to felsic melts is not an important cause of the spread in observed trace elements in zircon. Instead, we interpret differences in zircon geochemistry from single handsamples within the context of an evolving magma composition (e.g. see Section 4.1). Observed resorbed zircon cores in all samples except AD1 and AD2 may instead reflect antecrystic cores derived from a more localized portion of the magmatic system of similar bulk composition. We explore evolving zircon geochemistry from various samples within this paradigm below.

Plots of zircon Y/Hf, Eu/Eu*, Zr/Hf and Sc/Th (Fig. 5) and $\varepsilon_{Hf(T)}$ (Fig. 3A) versus U–Pb zircon dates record the evolution of the magmatic system from mafic to felsic. The sample the least affected by crustal contamination on the basis of $\varepsilon_{Hf(T)}$ in zircon ($+10$ to $+12$) is the quartz diorite AD7. Zircons from this sample are nearly equivalent in age, with the highest Sc/Th, lowest Y/Hf, steepest HREE patterns, and Zr/Hf similar to other mantle-derived zircons (Pupin, 2000; Figs. 4 and 5). Near mantle $\varepsilon_{Hf(T)}$values suggest this magma evolved primarily via fractionation and not crustal assimilation. Abundant plagioclase in the rock suggests that the highly variable zircon Eu/Eu* was generated within 10s of ka during plagioclase fractionation and ascent into the upper crust.

The two samples from the Blumone gabbro (AD1 and AD2) have indistinguishable zircon dates that fall within several 10 ka of each other, with the exception of two analyses from AD1 that are distinctly older around 42.2 Ma. AD1 and AD2 are pegmatitic gabbro samples that interfinger in places with megacrystic hornblende and in other places fill brittle fractures that cross-cut mafic and ultramafic rocks. Our zircon dates therefore represent the latest phase of crystallization of the Blumone gabbro and ultramafic units. Aspects of zircon geochemistry, such as extreme U and Th enrichment, are consistent with their origin as residual liquid from nearly complete crystallization of a gabbroic melt. However, moderate $\varepsilon_{Hf(T)}$ ($+5$ to $+7$) and low abundances of Y, the REE, and Hf and only minor Eu anomalies suggest that fractionation alone cannot explain these melts and also require crustal contamination, consistent with whole-rock Nd and Sr isotopes (Kagami et al., 1991).

Vacca tonalite samples AD3, AD5, and RdC3 show protracted growth of zircon spanning 300 ka between 42.15 and 41.85 Ma, with the duration of zircon growth in each sample increasing westward. Taken as a whole, all the trace element data from Vacca tonalite zircons show slight trends with time (Fig. 5), though there is considerable scatter in the data. Overall, zircon Eu anomaly becomes less negative with time, which is most obviously observed in sample RdC3 ($r^2=0.47$). This trend cannot be created by fractional crystallization of any phase, suggesting assimilation of either country rock or a more primitive magma into the parental Vacca tonalitic magma. In light of this, all other observed trends could also be a result of protracted assimilation and/or magma mixing over several hundred ka within an interconnected magmatic plumbing system. Ubiquitous mafic enclaves within the Vacca tonalite are evidence of magma mingling, and perhaps mixing at depth prior to intrusion or at the level of emplacement (Supplementary material Fig. S1; see discussion in Section 4.4).

The most prominent trends in trace elements with time come from sample AD12 of the Galliner granodiorite, whose $^{206}Pb/^{238}U$ zircon dates are distinctly younger than those from the Vacca tonalite, ranging from 41.87 ± 0.03 to 41.76 ± 0.03 Ma. These include decreasing $\varepsilon_{Hf(T)}$ ($+5$ to $+2$; $r^2=0.85$; Fig. 3A) and Eu/Eu* ($r^2=0.19$), and increasing Y/Hf ($r^2=0.81$), and Zr/Hf ($r^2=0.25$; Fig. 5). The trend in $\varepsilon_{Hf(T)}$ requires progressive assimilation of low $\varepsilon_{Hf(T)}$ melts or rocks with time, and this process could control the other trace element signatures as well. Fractional crystallization within a magma chamber could also evolve liquid compositions, though the scatter in trace element correlation diagrams (Fig. 4) shows that no one phase alone can account for the trends. For example, Y/Hf is expected to increase in a magma as a result of zircon crystallization (Fig. 5A) while Zr/Hf is expected to decrease (Linnen and Keppler, 2002; Reid et al., 2010). Based on the experimental partition coefficient data of Prowatke and Klemme (2005, 2006b), neither fractional crystallization of apatite nor titanite can be accountable for the observed trends in AD5. Therefore, we conclude that the trace element evolution observed in the Galliner granodiorite zircons is a result of AFC processes, showing that further detailed studies involving TIMS-TEA data combined with whole–rock and mineral geochemistry are promising avenues for future work.

4.3. Titanite U–Pb dates: recorders of crystallization, cooling, subsolidus growth?

We carried out U–Pb TIMS-TEA on titanite from five of the seven samples from this study. $^{206}Pb/^{238}U$ dates from AD3 and RdC3 are 0–300 ka younger than the youngest zircon dates for each sample, and titanite trace element patterns within each sample show little variation (Fig. 6). Limited experimental data from titanite (Cherniak, 1995) show that diffusion of both Sr and Nd is several orders of magnitude slower than that of Pb, corresponding to nominal closure temperatures of >900 °C for cooling rates of 10 °C/Ma and a grain radius of 1 mm. Given the fast cooling rates implied by overlapping zircon and titanite dates from these samples (using a nominal closure temperature for titanite of $\sim$600–700 °C; Cherniak, 1993), titanite geochemistry should reflect that of the magma it crystallized from given equilibrium partitioning. Petrographically, titanite from AD7 and AD3 primarily form euhedral to subhedral crystals along grain boundaries, supporting late saturation in a magma. In several locations, a second, younger population of anhedral titanite in AD7 is found overgrowing opaque phases and intergrown with chlorite. Mixing between these two populations could create the trends observed between titanite $^{206}Pb/^{238}U$ dates and geochemistry in AD7 (Fig. 6), also observed in samples AD5 and AD12, discussed below.

Titanite from Vacca tonalite sample AD5 and Galliner granodiorite sample AD12 are between 150 and 800 ka younger than zircon dates from the same sample (Figs. 2 and 6). As with sample AD7, titanite geochemistry shows correlations with time over

150–200 ka, and this is difficult to explain if the dates were recording slow cooling through Pb closure. Titanite dates either show no correlation (AD12) or are anti-correlated (AD5) with grain size, and therefore cannot be explained by differing diffusion dimensions. Petrographically, titanite from these samples predominantly form as anhedral overgrowths to oxide minerals, as fine grained clots associated with oxides and chlorite, and as large anhedral oikocrysts located along grain boundaries with inclusions of apatite and plagioclase. Therefore, petrographic, geochemical, and geochronologic data are most consistent with titanite formation in samples AD5 and AD12 during subsolidus alteration and/or fluid flow in these rocks. Continued magmatic activity produced the neighboring tonalite of Malga Listino and the leucotonalite of Cima di Vallone ca. 41.7 – 40.9 Ma (Schaltegger et al., 2009), and this may have provided magmatic fluids motivating subsolidus/metamorphic titanite crystallization in our samples.

In summary, U–Pb TIMS-TEA data can discern two different titanite-forming processes in the Lago della Vacca complex: magmatic titanite whose U–Pb dates record cooling beneath ca. 600–700 °C and late subsolidus growth of titanite (Fig. 6). U–Pb cooling dates from the magmatic population of titanite from samples AD7 and AD3 overlap with the zircon data, providing a minimum time for intrusion of the eastern side of the Lago della Vacca complex. These data also require the rocks were below the solidus ca. 42.0 Ma, slightly before the oldest zircon dates from the Galliner granodiorite.

4.4. Tempo of emplacement of the Lago della Vacca complex

In this section we explore the emplacement model for the LVC of John and Blundy (1993) outlined in Section 2, given our new geochronological and geochemical constraints provided by U–Pb TIMS-TEA. The prediction of this model, similar to ballooning models hypothesized for other plutons, is that the emplacement time of the LVC should young towards the center of the intrusion (i.e. the Galliner granodiorite). Though zircon U–Pb dates generally meet this expectation, determining the timing of emplacement from our zircon and titanite U–Pb data depends on the interpretation of the range in zircon crystallization ages observed for the inner, felsic lithologies (AD12, AD5, RdC3), corresponding to the Vacca tonalite and the Galliner granodiorite. Two endmember interpretations are possible: (1) that the entire LVC was emplaced very rapidly (10s of ka) and that the range in zircon dates from single samples reflects in situ crystallization for ~300 ka following emplacement; (2) that the youngest zircon dates from each sample record emplacement and older zircons from the same samples are antecrystic and transported from depth. The zircon and titanite U–Pb TIMS-TEA data provide three constraints that must be consistent with either model, namely that (1) older zircon from felsic samples were not inherited from mafic samples (Section 4.2), (2) that the oldest zircon from the Galliner granodiorite is ~200 ka younger than the oldest zircons in other samples (Fig. 2), and (3) that cooling ages from titanite in samples AD7 and AD3 require that the outer margins of the LVC had solidified immediately before the oldest zircons from the Galliner granodiorite had crystallized (Section 4.3).

The simpler of the two endmember models is model 1, suggesting rapid emplacement in <50 ka, because it allows for the concentric magmatic fabrics observed in the Vacca tonalite and Galliner granodiorite to have been created by forceful emplacement of the core of the pluton. In this model, zircon saturates in the ascending magma batches immediately prior to or during emplacement. The margins of the LVC crystallize zircon for 10s of ka during rapid cooling and solidification, while the core of the Vacca tonalite crystallizes zircon for up to 300 ka during protracted cooling. This predicts negligible mixing between the mafic margins and felsic core pulses, as required by zircon geochemistry and field observation (Brack, 1983; John and Blundy, 1993), implying that observed heterogeneous magma compositions were created at depth. This model also predicts that the evolving zircon geochemistry and Hf isotopic composition in single Vacca tonalite handsamples were created at the level of emplacement through AFC processes. The main difficulty with this model is that melt is required to be present in the Vacca tonalite following emplacement for 100s of ka, inconsistent with the simple cooling calculations performed by John and Blundy (1993), which show that a single, LVC intrusion should fully crystallize in ~60 ka. Another difficulty is that if the Galliner granodiorite intruded synchronously with the Vacca tonalite, it would have likely saturated with zircon immediately, given zircon saturation temperatures in granodioritic magmas are typically higher than those in more mafic magmas (Watson and Harrison, 1983), whereas the oldest zircons from the Galliner granodiorite (AD12) are 200 ka younger than the oldest zircons from the Vacca tonalite (AD3, RdC3, AD5).

Endmember model 2 proposes a much longer timescale of intrusion, whereby magma pulses intrude incrementally into the core of the LVC over a time period of 300 ka. In this model, each successive pulse cools and solidifies rapidly following emplacement, where emplacement is recorded by the youngest zircon from each hand sample. This model predicts that zircon for the outer units saturates during ascent and emplacement and that zircon in the inner felsic units saturates in a deeper part of the magmatic system and crystallizes for 100s of ka during AFC processes prior to final emplacement. As such, ascending magma pulses carry with them antecrystic zircon with heterogeneous trace element compositions. The difficulty of this model arises from the titanite cooling ages from the margins of the pluton. Given that generating magmatic fabrics requires the presence of $>5\%$ melt (Paterson et al., 1998) and the solidus of a tonalitic magma is greater than the closure temperature of Pb in titanite (~600 °C; Cherniak, 1993), magmatic fabrics in the margins of the Vacca tonalite need to have been created prior to the emplacement of the inner pulses. This is difficult to envision given the concentric geometry of the system, which suggests a genetic relationship between the core of the pluton and magmatic fabrics in the rim (John and Blundy, 1993).

A hybrid between the two endmember models described above may be able to overcome their respective difficulties, and this model is shown conceptually in Fig. 7. The Blumone gabbro (samples AD1 and AD2) and the marginal quartz diorite (AD7) intrude ca. 42.2–42.06 Ma (Fig. 7A). Early pulses of the Vacca tonalite intrude forcefully ca. 42.1 Ma, translating the mafic units to the east, generating magmatic fabrics in these units during dextral shearing on the southern margin of the Blumone tonalites and diorites (Fig. 7B; John and Blundy, 1993). Early pulses of Vacca tonalite saturate with zircon upon ascent and emplacement while later pulses may also entrain antecrystic Vacca zircon from depth or from slightly younger pulses at the emplacement level. Continued intrusion of the Vacca tonalite over several hundred ka provides the opportunity for magma mixing (at depth and/or at the emplacement level) recorded by zircon geochemistry and may also provide sufficient heat to maintain a significant percent melt for this period of time (Fig. 7C). Finally, during the waning stages of crystallization of the Vacca tonalite ca. 41.9 Ma, forceful intrusion of the Galliner granodiorite imposes sufficient radial stress to create the concentric magmatic fabrics in the Vacca tonalite and early batches of Galliner magma (Fig. 7D). Evolution of zircon geochemistry within the Galliner granodiorite (sample AD12) over ~150 ka may have been generated at depth prior to intrusion or post-emplacement through mixing/assimilation of a low ε_{Hf} host rock or evolved melt.

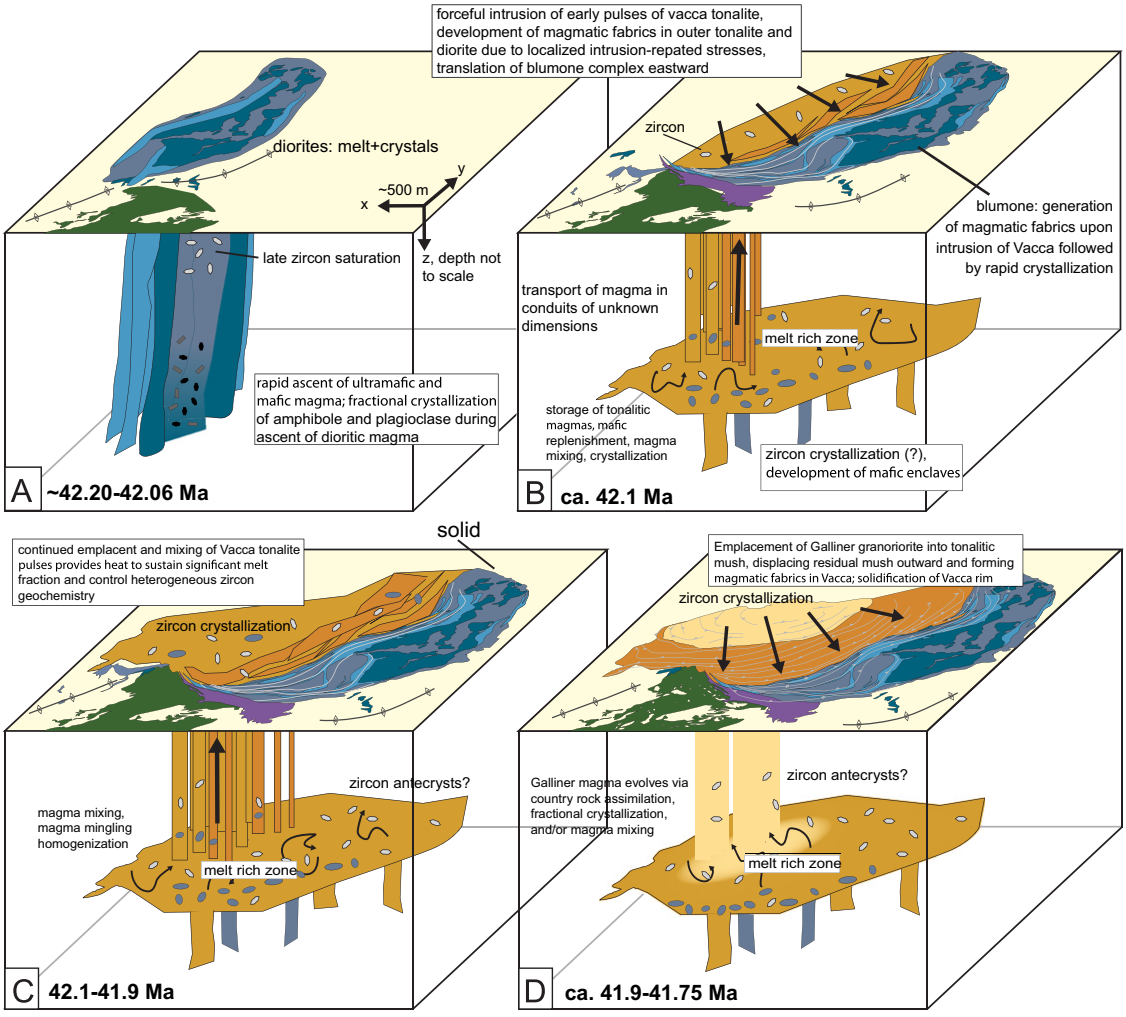

Fig. 7. Simplified intrusion model for the Lago della Vacca complex. A–D represent a pseudo-3D time series for the sequence of intrusions determined by U–Pb TIMS-TEA. Top of the cube represents the outcrop pattern, and the depth is not to scale. Feeder conduits and geometry of magma reservoirs at depth is not well constrained, as discussed in the text. Conduits are drawn as thin dikes simply to remove clutter from the 3D cartoon. (A) Ultramafic to mafic mantle melts ascend rapidly through the crust to emplacement level. Fractional crystallization during depressurization results in dioritic magmas with little to no crustal assimilation. Late gabbroic pegmatites form in Blumone complex, mixing with crustal-derived fluid. (B) First stage of pulsed intrusion of Vacca tonalite. Development of margin parallel magmatic fabrics in Blumone diorites and tonalites due to forceful intrusion of Vacca tonalite. (C) Continued magmatic activity in tonalitic magma reservoirs and intrusion of Vacca tonalite. Mixing and mingling of magmas at depth and/or at level of emplacement result in evolving zircon geochemistry and source of zircon antecrysts. Tonalitic pulses also provide additional heat to slow down cooling of Vacca at level of emplacement. (D) Lower magma reservoir undergoes crustal assimilation, continued fractional crystallization and development of granodioritic magma, which intrudes central Vacca as crystal mush. Forceful intrusion of the Galliner granodiorite provides "ballooning" related stress causing concentric magmatic fabrics in Vacca tonalite and Galliner granodiorite. Final stage includes the intrusion of units directly to the north (see Fig. 2), and continued fluid migration and growth of subsolidus titanite until ca. 41 Ma.

The success of the proposed model is dependent on whether the thermal budget of the system is sufficient to keep the Vacca tonalite above the solidus for several hundred ka and also on whether the magma mixing recorded in Vacca zircon geochemistry could have happened at the level of emplacement. More detailed thermal modeling could help constrain the thermal evolution of the system, though recent models of pulsed intrusion into the upper crust suggest this is possible (e.g. Annen, 2011). Field observation in the Vacca tonalite over the course of this study and that of Brack (1985) observed ubiquitous mafic enclaves within the Vacca tonalite, but little evidence for magma mixing at the outcrop scale. However, descriptions of disaggregated synplutonic dikes within the Vacca (John and Blundy, 1993;) may be indication that coexistence and mixing of mafic and more felsic magmas at the level of emplacement was an important process and thus could explain the geochemical record in Vacca tonalite zircon.

Classic ballooning models argue that the increased magmatic strain observed at the margins of the pluton is caused by radial expansion due to a central feeder dike (e.g. Bateman, 1985; Ramsay, 1989; John and Blundy, 1993; Paterson and Vernon, 1995). An alternative "nested diapir" model for the emplacement of plutons with similar geometries, kinematics, and host rock relationships was discussed by Paterson and Vernon (1995). This model also predicts center-younging pulsed intrusion, consistent with our geochronological data, but also involves substantial downflow of marginal magmas during emplacement of more central units. Our data show that the margins of the LVC were solid and $<600\,^{\circ}C$ immediately prior to the intrusion of the Galliner granodiorite, providing temporal constraints on the observed supersolidus strain patterns described by John and Blundy (1993) and limiting downflow of marginal units during core emplacement. Our data therefore place important constraints on strain accumulation as a function of time and should figure into more mechanistic models for balloon-like pluton emplacement. Another potential difference between the nested diapir model and that pictured in Fig. 7 is the feeder system, which we have depicted as a series of dikes of unknown size as

opposed to a more continuous magmatic system at depth. Though topography in the Adamello region allows ~2 km vertical exposure, the deep interior of the magmatic system remains hidden, and the geometry at depth pictured in Fig. 7 remains unconstrained. Further investigation of middle to lower crustal intrusions in combination with high-precision geochronology and accompanied mineral geochemistry provided by U–Pb TIMS-TEA will provide a much richer understanding of the links between upper crustal intrusions and their source regions.

5. Conclusions

High-precision zircon U–Pb ID-TIMS geochronology from the Lago della Vacca complex (LVC), Adamello batholith, show that zircon crystallization in single handsamples occurred over <20 ka to >300 ka. We use these data in combination with geochemistry of zircon from the same dated zircons (U–Pb TIMS-TEA) to show that early mafic pulses of magma ascended through the crust with little or no assimilation of crustal material. Zircon from later, more felsic, magmas record magma evolution through AFC processes over 300 ka prior to final solidification.

Zircon U–Pb TIMS-TEA data can be used to fingerprint antecrystic versus autocrystic zircon in magmatic systems, providing insight into magmatic plumbing systems and lifetimes. These data, combined with field observation and whole-rock geochemistry can also be used to test whether U–Pb zircon dates record emplacement of magma or post-emplacement crystallization.

Titanite TIMS-TEA data reveal two populations of titanite in the LVC: magmatic titanite that record cooling through its closure temperature (~600 °C), and subsolidus titanite that record low-T metamorphic growth, potentially facilitated by late magmatic fluids in the system.

Our data provide a high-precision timescale and thermal constraints that inform balloon-like emplacement models for the LVC. For example, such data are important for constraining formation times of magmatic fabrics in relation to emplacement of magma pulses, which are dependent on the thermal and rheological state of the system. Similar datasets for other proposed ballooning magmatic systems are necessary to further describe processes of mass and heat transfer between magma and wall-rock and understand how space is created during magma ascent and emplacement.

Acknowledgement

The authors would like to thank J. Blundy, M. Schmitz, and the AE T. Elliot for insightful reviews that greatly improved this manuscript. A. Skopelitis and M. Senn are thanked for assistance with sample preparation and lab upkeep at the University of Geneva. This work was supported by the Swiss National Science Foundations.

Appendix A. Supporting information

Supplementary data associated with this article can be found in the online version at http://dx.doi.org/10.1016/j.epsl.2012.08.019.

References

Adam, J., Green, T., 2006. Trace element partitioning between mica- and amphibole-bearing garnet lherzolite and hydrous basanitic melt: 1. Experimental results and the investigation of controls on partitioning behaviour. Contrib. Miner. Petrol. 152, 1–17.

Annen, C., 2011. Implications of incremental emplacement of magma bodies for magma differentiation, thermal aureole dimensions and plutonism–volcanism relationships. Tectonophysics 500, 3–10 10.106/j.tecto.2009.04.010.

Annen, C., Blundy, J.D., Sparks, R.S.J., 2006. The genesis of intermediate and silicic magmas in deep crustal hot zones. J. Petrol. 47, 505–539, http://dx.doi.org/10.1093/petrology/egi084.

Bachmann, O., Schoene, B., Schnyder, C., Spikings, R., 2010. The 40Ar/39Ar and U/Pb dating of young rhyolites in the Kos-Nisyros volcanic complex, Eastern Aegean Arc, Greece: age discordance due to excess 40Ar in biotite. Geochem. Geophys. Geosyst. 11, Q0AA08, http://dx.doi.org/10.1029/2010gc003073.

Bacon, C.R., Lowenstern, J.B., 2005. Late Pleistocene granodiorite source for recycled zircon and phenocrysts in rhyodacite lava at Crater Lake, Oregon. Earth Planet. Sci. Let. 233, 277–293.

Brack, P.B., 1983. Multiple intrusions - examples from the Adamello batholith (Italy) and their significance on the mechanism of intrusion. Mem. Soc. Geol. Ital. 26, 145–157.

Barth, A.P., Wooden, J.L., 2010. Coupled elemental and isotopic analyses of polygenetic zircons from granitic rocks by ion microprobe, with implications for melt evolution and the sources of granitic magmas. Chem. Geol. 277, 149–159.

Bateman, R., 1985. Aureole deformation by flattening around a diapir during in situ ballooning: the cannibal creek granite. J. Geol. 93, 293–310.

Bédard, J.H., 2006. A catalytic delamination-driven model for coupled genesis of Archaean crust and sub-continental lithospheric mantle. Geochim. Cosmochim. Acta 70, 1188–1214.

Belousova, E.A., Griffin, W.L., O'Reilly, S.Y., 2006. Zircon crystal morphology, trace element signatures and hf isotope composition as a tool for petrogenetic modelling: examples from eastern Australian granitoids. J. Petrol. 47, 329–353, http://dx.doi.org/10.1093/petrology/egi077.

Belousova, E.A., Griffin, W.L., O'Reilly, S.Y., Fisher, N.I., 2002. Igneous zircon: trace element composition as an indicator of source rock type. Contrib. Miner. Petrol. 143, 602–622, http://dx.doi.org/10.1007/s00410-002-0364-7.

Brack, P.B., 1985. Multiple intrusions – examples from the Adamello batholith (Italy) and their significance on the mechanism of intrusion. Mem. Soc. Geol. Italy 26, 145–157.

Brown, M., 2007. Crustal melting and melt extraction, ascent and emplacement in orogens: mechanisms and consequences. J. Geol. Soc. 164, 709–730.

Cavosie, A.J., Wilde, S.A., Liu, D., Weiblen, P.W., Valley, J.W., 2004. Internal zoning and U–Th–Pb chemistry of Jack Hills detrital zircons: a mineral record of early archean to mesoproterozoic (4348–1576 Ma) magmatism. Precam. Res. 135, 251–279.

Charlier, B.L.A., Wilson, C.J.N., 2010. Chronology and evolution of caldera-forming and post-caldera magma systems at okataina volcano, New Zealand from zircon U–Th model-age spectra. J. Petrol. 51, 1121–1141.

Charlier, B.L.A., Wilson, C.J.N., Lowenstern, J.B., Blake, S., Van Calstren, P.W., Davidson, J.P., 2005. Magma generation at a large hyperactive silicic volcano (Taupo, New Zealand) revealed by U—Th and U—Pb systematics in zircons. J. Pet., 46, 3–32, http://dx.doi.org/10.1093/petrology/egh060.

Cherniak, D.J., 1993. Lead diffusion in titanite and preliminary results on the effects of radiation damage on Pb transport. Chem. Geol. 110, 177–194.

Cherniak, D.J., 1995. Sr and Nd diffusion in titanite. Chem. Geol. 125, 219–232.

Claiborne, L., Miller, C., Wooden, J., 2010. Trace element composition of igneous zircon: a thermal and compositional record of the accumulation and evolution of a large silicic batholith, Spirit Mountain, Nevada. Contrib. Miner. Petrol. 160, 511–531, http://dx.doi.org/10.1007/s00410-010-0491-5.

Claiborne, L.L., Miller, C.F., Walker, B.A., Wooden, J.L., Mazdab, F.K., Bea, F., 2006. Tracking magmatic processes through Zr/Hf ratios in rocks and Hf and Ti zoning in zircons: an example from the Spirit Mountain batholith, Nevada. Mineral. Mag. 70, 517–543.

Coleman, D.S., Gray, W., Glazner, A.F., 2004. Rethinking the emplacement and evolution of zoned plutons: geochronologic evidence for incremental assembly of the Tuolumne Intrusive Suite, California 32, 433–436Geology 32, 433–436.

Cortecci, G., Del Moro, A., Leone, G., Pardini, G.C., 1979. Correlation between strontium and oxygen isotopic compositions of rocks from the Adamello massif (Northern Italy). Contrib. Mineral. Petrol. 68, 421–427.

Crowley, J.L., Schoene, B., Bowring, S.A., 2007. U–Pb dating of zircon in the Bishop Tuff at the millennial scale. Geology 35, 1123–1126, http://dx.doi.org/10.1130/G24017A.

Cruden, A.R., 1990. Flow and fabric development during the diapiric rise of magma. J. Geol. 98, 681–698.

Del Moro, A., Ferrara, G., Tonarini, S., Callegari, E., 1985a. Rb-Sr systematics on rocks from the Adamello batholith (southern Alps). Mem. Soc. Geol. Italy 26, 261–284.

Del Moro, A., Pardini, G., Quercioli, C., Villa, I.M., Callegari, E., 1985b. Rb/Sr and K/Ar chronology of adamello granitoids, southern Alps. Mem. Soc. Geol. Italy 26, 285–299.

Glazner, A.F., Bartley, J.M., 2006. Is stoping a volumetrically significant pluton emplacement process? Geol. Soc. Am. Bull. 118, 1185–1195, http://dx.doi.org/10.1130/B25738.1.

Glazner, A.F., Bartley, J.M., Coleman, D.S., Gray, W., Taylor, R.Z., 2004. Are plutons assembled over millions of year by amalgamation from small magma chambers? Geol. Soc. Am. Today 14, 4–11.

Griffin, W.L., Wang, W., Jackson, S.E., Pearson, N.J., O'Reilly, S.Y., Xu, X., Zhou, X., 2002. Zircon chemistry and magma mixing, SE China: In-situ analysis of Hf isotopes, Tonglu and Pingtan igneous complexes. Lithos 61, 237–269.

Grunder, A.L., Klemetti, E.W., Feeley, T.C., McKee, C.M., 2006. Eleven million years of arc volcanism at the Aucanquilcha Volcanic Cluster, northern Chilean Andes: implications for the life span and emplacement of plutons. Earth Environ. Sci. Trans. R. Soc. Edinburgh 97, 415–436.

Hanchar, J.M., van Westrenen, W., 2007. Rare earth element behavior in zircon-melt systems. Elements 3, 37–42.
Hofmann, A., Valley, J., Watson, E., Cavosie, A., Eiler, J., 2009. Sub-micron scale distributions of trace elements in zircon. Contrib. Mineral. Petrol. 158, 317–335.
Hollister, L.S., Crawford, M.L., 1986. Melt-enhanced deformation: a major tectonic process. Geology 14, 558–561.
Hoskin, P.W.O., Schaltegger, U., 2003. The composition of zircon and igneous and metamorphic petrogenesis. Rev. Mineral. Geochem. 53, 27–62, http://dx.doi.org/10.2113/0530027.
Hutton, D.H.W., Dempster, T.J., Brown, P.E., Becker, S.D., 1990. A new mechanism of granite emplacement: intrusion in active extensional shear zones. Nature 343, 452–456.
John, B.E., Blundy, J.D., 1993. Emplacement-related deformation of granitoid magmas, southern Adamello Massif, Italy. Geol. Soci. Am. Bull. 105, 1517–1541.
John, B.E., Stünitz, H., 1997. Magmatic fracturing and small-scale melt segregation during pluton emplacement: evidence from the Adamello Massif (Italy). In: Bouchez, J.L., (Ed.), Granite: From Segregation of Melt to Emplacement Fabrics. Kluwer Academic Publishers, pp. 55–74.
Kagami, H., Ulmer, P., Hansmann, W., Dietrich, V., Steiger, R.H., 1991. Nd–Sr isotopic and geochemical characteristics of the southern Adamello (Northern Italy) intrusives: implications for crustal versus mantle origin. J. Geophys. Res. 96, 14331–14346.
Laube, N., Springer, J., 1998. Crustal melting by ponding of mafic magmas: a numerical model. J. Volcanol. Geotherm. Res. 81, 19–35.
Linnen, R.L., Keppler, H., 2002. Melt composition control of Zr/Hf fractionation in magmatic processes. Geochim. Cosmochim. Acta 66, 3293–3301.
Lissenberg, C.J., Rioux, M., Shimizu, N., Bowring, S.A., Mével, C., 2009. Zircon dating of oceanic crustal accretion. Science 323, 1048–1050, http://dx.doi.org/10.1126/science.1167330.
Matzel, J.P., Bowring, S.A., Miller, R.B., 2006. Timescales of pluton construction at differing crustal levels: examples from the Mount Stuart and Tenpeak intrusions, North Cascades, WA. Geol. Soc. Am. Bull. 118, 1412–1430, http://dx.doi.org/10.1130/B25923.1.
Memeti, V., Paterson, S., Matzel, J., Mundil, R., Okaya, D., 2010. Magmatic lobes as "snapshots" of magma chamber growth and evolution in large, composite batholiths: an example from the Tuolumne intrusion, Sierra Nevada, California 122, 1912–1931, http://dx.doi.org/10.1130/B30004Geol. Soc. Am. Bull. 122, 1912–1931, http://dx.doi.org/10.1130/B30004.
Michel, J., Baumgartner, L., Putlitz, B., Schaltegger, U., Ovtcharova, M., 2008. Incremental growth of the Patagonian Torres del Paine laccolith over 90 k.y. Geology 36, 459–462.
Miller, J.S., Matzel, J.P., Miller, C.F., Burgess, S.D., Miller, R.B., 2007. Zircon growth and recycling during the assembly of large, composite arc plutons. J. Volcanol. Geotherm. Res. 167, 282–299.
Paterson, S.R., Pignotta, G.S., Farris, D., Memeti, V., Miller, R.B., Vernon, R.H., 2008. Is stoping a volumetrically significant pluton emplacement process?: Discussion. Geol. Soc. Am. Bull. 120, 1075–1079.
Paterson, S.R., Fowler, T.K.J., Schmidt, K.L., Yoshinobu, A.S., Yuan, E.S., Miller, R.B., 1998. Interpreting magmatic fabric patterns in plutons. Lithos. 44, 53–82.
Paterson, S.R., Vernon, R.H., 1995. Bursting the bubble of ballooning plutons: a return to nested diapirs emplaced by multiple processes. Geol. Soc. Am. Bull. 107, 1356–1380.
Prowatke, S., Klemme, S., 2005. Effect of melt composition on the partitioning of trace elements between titanite and silicate melt. Geochim. Cosmochim. Acta 69, 695–709.
Prowatke, S., Klemme, S., 2006a. Rare earth element partitioning between titanite and silicate melts: Henry's law revisited. Geochim. Cosmochim. Acta 70, 4997–5012.
Prowatke, S., Klemme, S., 2006b. Trace element partitioning between apatite and silicate melts. Geochim. Cosmochim. Acta 70, 4513–4527.
Pupin, J.-P., 2000. Granite genesis related to geodynamics from Hf–Y in zircon. Trans. R. Soc. Edinburgh Earth Sci. 91, 245–256.
Ramsay, J.G., 1989. Emplacement kinematics of a granite diapir: the Chindamora batholith, Zimbabwe. J. Struct. Geol. 11, 191–209.
Reid, M., Vazquez, J., Schmitt, A., 2010. Zircon-scale insights into the history of a supervolcano, Bishop Tuff, long valley, California, with implications for the Ti-in-zircon geothermometer. Contrib. Mineral.Petrol. , http://dx.doi.org/10.1007/s00410-010-0532-0.
Reid, M.R., Coath, C.D., 2000. In situ U–Pb ages of zircons from the Bishop Tuff: no evidence for long crystal residence times. Geology 28, 443–446.
Rubatto, D., Hermann, J., 2007. Experimental zircon/melt and zircon/garnet trace element partitioning and implications for the geochronology of crustal rocks. Chem. Geol. 241, 38–61.
Sandiford, M., McLaren, S., Neumann, N., 2002. Long-term thermal consequences of the redistribution of heat-producing elements associated with large-scale granitic complexes. J. Metamorphic Geol. 20, 87–98.
Sano, Y., Terada, K., Fukuoka, T., 2002. High mass resolution ion microprobe analysis of rare earth elements in silicate glass, apatite and zircon: lack of matrix dependency. Chem. Geol. 184, 217–230.
Schaltegger, U., Brack, P.B., Ovtcharova, M., Peytcheva, I., Schoene, B., Stracke, A., Bargossi, G.M., 2009. Zircon U, Pb, Th, and Hf isotopes record up to 700 kyrs of magma fractionation and crystallization in a composite pluton (Adamello batholith, N Italy). Earth Planet. Sci. Lett. 286, 208–218.
Schmitt, A.K., Stockli, D.F., Lindsay, J.M., Robertson, R., Lovera, O.M., Kislitsyn, R., 2010. Episodic growth and homogenization of plutonic roots in arc volcanoes from combined U–Th and (U–Th)/He zircon dating. Earth Planet. Sci. Lett. 295, 91–103.
Schoene, B., Crowley, J.L., Condon, D.C., Schmitz, M.D., Bowring, S.A., 2006. Reassessing the uranium decay constants for geochronology using ID-TIMS U-Pb data. Geochim. Cosmochim. Acta 70, 426–445.
Schoene, B., Bowring, S.A., 2010. Rates and mechanisms of mesoarchean magmatic arc construction, eastern Kaapvaal craton, Swaziland 122, 408–429, http://dx.doi.org/10.1130/B26501.1.
Schoene, B., Guex, J., Bartolini, A., Schaltegger, U., Blackburn, T.J., 2010a. Correlating the end-Triassic mass extinction and flood basalt volcanism at the 100,000-year level. Geology 38, 387–390, http://dx.doi.org/10.1130/G30683.1.
Schoene, B., Latkoczy, C., Schaltegger, U., Gunther, D., 2010b. A new method integrating high-precision U–Pb geochronology with zircon trace element analysis (U–Pb TIMS-TEA). Geochim. Cosmochim. Acta 74, 7144–7159.
Stacey, J.C., Kramers, J.D., 1975. Approximation of terrestrial lead isotope evolution by a two-stage model. Earth Planet. Sci. Lett. 26, 207–221.
Thomas, J.B., Bodnar, R.J., Shimizu, N., Sinha, A.K., 2002. Determination of zircon/melt trace element partition coefficients from SIMS analysis of melt inclusions in zircon. Geochim. Cosmochim. Acta 66, 2887–2901.
Ulmer, P., Callegari, E., Sonderegger, U.C., 1985. Genesis of the mafic and ultramafic rocks and their genetical relations to the tonalitic-trondhjemitic granitoids of the southern part of the Adamello batholith, (Northern Italy). Mem. Soc. Geol. Italy 26, 171–222.
Vazquez, J.A., Reid, M.R., 2002. Time scales of magma storage and differentiation of voluminous high-silica rhyolites at Yellowstone caldera, Wyoming. Contrib. Miner. Petrol. 144, 274–285.
Vigneresse, J.-L., 1999. Should felsic magmas be considered as tectonic objects, just like faults or folds? J. Struct. Geol. 21, 1125–1130.
Watson, E.B., Harrison, T.M., 1983. Zircon saturation revisited: temperature and composition effects in a variety of crustal magma types. Earth Planet. Sci. Lett. 64, 295–304.
Wilson, C.J.N., Charlier, B.L.A., 2009. Rapid rates of magma generation at contemporaneous magma systems, Taupo Volcano, New Zealand: insights from U–Th model-age spectra in zircons. J. Petrol. 50, 875–907.

Supplementary Table 1: U-Pb isotopic data

Sample (a)	Epsilon Hf(T) (b)	Th/U (c)	Pb*/Pb$_c$ (e)	Pb$_c$ (pg) (d)	^{206}Pb/^{204}Pb (e)	^{208}Pb/^{206}Pb (f)	^{207}Pb/^{206}Pb (f)	% err (g)	^{207}Pb/^{235}U (f)	% err (g)	^{206}Pb/^{238}U (f)	% err (g)	corr. coef.	^{207}Pb/^{206}Pb (h)	± (g)	^{207}Pb/^{235}U (h)	± (g)	^{206}Pb/^{238}U (h)	± (g)
		Radiogenic Isotope Ratios												Isotopic Ages (Ma)					
AD1	(N 45˚57'30.1"/E 10˚27'29.5")																		
z5		1.13	133	0.37	6877	0.36	0.046839	0.072	0.042273	0.090	0.006546	0.049	0.602	41.05	1.73	42.04	0.04	42.06	0.02
z4	-3.7	0.70	7.3	5.87	435	0.23	0.047107	0.651	0.042519	0.690	0.006546	0.050	0.785	54.67	15.53	42.28	0.29	42.06	0.02
z6		0.91	120	0.42	6540	0.29	0.046919	0.072	0.042363	0.084	0.006548	0.037	0.530	45.11	1.72	42.13	0.03	42.08	0.02
z2	5.9	0.85	39	0.50	2189	0.27	0.047004	0.193	0.042448	0.207	0.006550	0.037	0.464	49.42	4.60	42.21	0.09	42.08	0.02
z1	4.7	0.90	23	0.66	1278	0.29	0.046988	0.387	0.042450	0.415	0.006552	0.069	0.469	48.62	9.23	42.21	0.17	42.10	0.03
z8		0.88	64	0.41	3530	0.28	0.046999	0.133	0.042470	0.150	0.006554	0.052	0.475	49.20	3.18	42.23	0.06	42.11	0.02
z3	5.2	0.82	93	0.71	5176	0.27	0.046967	0.089	0.042507	0.119	0.006564	0.074	0.668	47.55	2.12	42.27	0.05	42.18	0.03
z7		0.64	13	0.61	748	0.20	0.046436	0.684	0.042092	0.737	0.006574	0.145	0.448	20.34	16.41	41.86	0.30	42.24	0.06
AD2	(N 45˚57'33.9"/E 10˚27'27.6")																		
z2		0.99	4.5	8.21	259	0.32	0.047059	0.838	0.042479	0.889	0.006547	0.090	0.600	52.22	19.98	42.24	0.37	42.07	0.04
z4	4.7	1.22	805	0.66	40755	0.39	0.046836	0.017	0.042288	0.095	0.006548	0.093	0.983	40.87	0.41	42.06	0.04	42.08	0.04
z8		1.63	234	0.53	10858	0.52	0.046872	0.043	0.042322	0.066	0.006549	0.049	0.766	42.70	1.02	42.09	0.03	42.08	0.02
z7		0.97	51	0.81	2745	0.31	0.046990	0.152	0.042431	0.165	0.006549	0.039	0.444	48.70	3.63	42.19	0.07	42.08	0.02
z6		0.76	16	0.91	929	0.24	0.046837	0.445	0.042304	0.473	0.006551	0.050	0.596	40.92	10.64	42.07	0.19	42.09	0.02
z1	6.3	1.34	37	1.99	1831	0.43	0.046927	0.214	0.042385	0.230	0.006551	0.043	0.457	45.49	5.11	42.15	0.10	42.09	0.02
z5		1.53	378	0.47	17892	0.49	0.046846	0.028	0.042316	0.053	0.006551	0.043	0.841	41.40	0.68	42.08	0.02	42.09	0.02
z3	6.6	1.13	2.9	33.6	172	0.37	0.047309	0.559	0.042759	0.583	0.006555	0.093	0.336	64.86	13.30	42.51	0.24	42.12	0.04
AD3	(N 45˚57'53.9"/E 10˚27'6.8")																		
s1		3.65	1.6	74.3	71	1.17	0.046960	1.371	0.042107	1.386	0.006503	0.045	0.330	47.21	32.76	41.88	0.57	41.80	0.02
s2		3.42	1.4	70.8	67	1.11	0.047528	1.433	0.042617	1.445	0.006503	0.045	0.279	75.85	34.04	42.38	0.60	41.80	0.02
s3		3.83	1.2	143.5	58	1.23	0.047132	2.482	0.042324	2.564	0.006513	0.121	0.696	55.94	59.19	42.09	1.06	41.87	0.05
z9	4.6	0.66	6.1	0.95	373	0.21	0.046950	1.186	0.042295	1.256	0.006534	0.082	0.864	46.67	28.31	42.06	0.52	41.98	0.03
z2	-0.1	0.67	1.7	2.19	116	0.22	0.048448	3.849	0.043645	4.082	0.006534	0.237	0.986	121.20	90.60	43.38	1.73	41.98	0.10
z10	2.7	0.75	15	0.94	890	0.24	0.047050	0.479	0.042403	0.508	0.006536	0.047	0.658	51.77	11.42	42.17	0.21	42.00	0.02
z4	1.2	0.64	44	0.49	2565	0.21	0.046940	0.182	0.042306	0.203	0.006537	0.064	0.462	46.18	4.35	42.07	0.08	42.00	0.03
z5	0.3	0.83	6.0	1.01	348	0.27	0.047467	1.412	0.042830	1.497	0.006544	0.101	0.849	72.80	33.55	42.58	0.62	42.05	0.04
z7	1.8	0.75	14	0.74	805	0.24	0.046995	0.536	0.042408	0.569	0.006545	0.057	0.617	48.98	12.78	42.17	0.23	42.05	0.02
z8		0.74	4.8	0.99	292	0.24	0.046594	1.707	0.042055	1.807	0.006546	0.130	0.788	28.47	40.88	41.83	0.74	42.06	0.05
z11	7.5	0.65	16	0.89	925	0.21	0.047060	0.470	0.042493	0.500	0.006549	0.061	0.542	52.26	11.20	42.26	0.21	42.08	0.03
z6	2.4	0.81	4.8	0.67	286	0.26	0.046825	1.533	0.042296	1.625	0.006551	0.128	0.735	40.32	36.64	42.06	0.67	42.09	0.05
z1	7.7	1.01	3.2	1.14	185	0.33	0.048185	2.609	0.043635	2.766	0.006568	0.169	0.933	108.37	61.57	43.37	1.17	42.20	0.07
z3	1.5	0.69	53	0.49	3071	0.22	0.047140	0.137	0.043399	0.149	0.006677	0.035	0.446	56.32	3.26	43.14	0.06	42.90	0.01
AD5	(N 45˚57'18.0"/E 10˚24'27.0")																		
s1		1.74	2.9	32.6	150	0.56	0.047016	0.572	0.041538	0.583	0.006408	0.035	0.332	50.04	13.65	41.32	0.24	41.17	0.01
s2		1.32	2.6	43.3	147	0.42	0.046631	0.666	0.041068	0.684	0.006387	0.062	0.339	30.38	15.94	40.87	0.27	41.05	0.03
s3		1.00	2.1	63.6	133	0.32	0.047420	0.608	0.041723	0.614	0.006381	0.037	0.201	70.44	14.44	41.51	0.25	41.01	0.01
z11	1.3	0.91	3.4	1.15	201	0.30	0.047698	2.149	0.042837	2.277	0.006514	0.139	0.931	84.31	50.93	42.59	0.95	41.85	0.06
z5	0.5	0.80	15	0.47	844	0.26	0.046971	0.505	0.042224	0.536	0.006520	0.047	0.681	47.77	12.06	41.99	0.22	41.89	0.02
z9	3.1	1.03	24	0.62	1264	0.33	0.046939	0.328	0.042208	0.349	0.006522	0.038	0.585	46.13	7.83	41.98	0.14	41.91	0.02
z2	1.7	0.49	3.7	0.71	243	0.16	0.047582	1.826	0.042811	1.935	0.006525	0.120	0.911	78.52	43.32	42.56	0.81	41.93	0.05
z10	1.6	0.69	13	1.12	739	0.22	0.046857	0.598	0.042221	0.634	0.006535	0.059	0.646	41.92	14.28	41.99	0.26	41.99	0.02
z3	1.4	0.73	38	0.41	2173	0.23	0.047044	0.243	0.042403	0.263	0.006537	0.058	0.446	51.46	5.79	42.17	0.11	42.00	0.02
z8		0.90	1.7	0.83	111	0.29	0.046934	4.359	0.042309	4.611	0.006538	0.258	0.979	45.86	104.07	42.08	1.90	42.01	0.11
z7	-0.4	0.78	1.8	1.02	118	0.26	0.048900	3.977	0.044187	4.217	0.006554	0.251	0.961	143.02	93.24	43.90	1.81	42.11	0.11
z6	-0.4	0.55	1.1	2.31	85	0.19	0.050264	5.580	0.045491	5.931	0.006564	0.355	0.989	207.22	129.30	45.17	2.62	42.18	0.15
z4	2.4	0.58	30	0.49	1784	0.19	0.047843	0.267	0.044818	0.288	0.006794	0.060	0.452	91.50	6.32	44.52	0.13	43.65	0.03
AD7	(N 45˚57'51.0"/E 10˚26'28.6")																		
s1		5.27	1.1	7.92	49	1.66	0.046243	3.539	0.041506	3.682	0.006510	0.190	0.762	10.31	85.17	41.29	1.49	41.83	0.08
s2		6.01	2.5	7.21	82	1.89	0.046115	1.807	0.041486	1.888	0.006525	0.109	0.759	3.62	43.54	41.27	0.76	41.92	0.05
s3		1.00	2.1	63.5	133	0.32	0.047420	0.607	0.041730	0.614	0.006382	0.037	0.201	70.44	14.44	41.51	0.25	41.01	0.01
z5	10.5	0.66	11	0.49	641	0.21	0.047086	0.675	0.042502	0.715	0.006546	0.051	0.800	53.62	16.08	42.26	0.30	42.06	0.02
z2	10.0	0.67	14	0.51	801	0.21	0.046802	0.541	0.042249	0.574	0.006547	0.054	0.646	39.14	12.92	42.02	0.24	42.07	0.02
z6	11.4	0.64	17	0.51	991	0.21	0.046973	0.447	0.042422	0.475	0.006550	0.046	0.630	47.83	10.68	42.19	0.20	42.09	0.02
z1	10.5	0.57	30	0.44	1777	0.18	0.046890	0.258	0.042356	0.283	0.006551	0.074	0.447	43.62	6.17	42.12	0.12	42.10	0.03
z3	10.9	0.65	69	0.47	4036	0.21	0.046930	0.117	0.042400	0.140	0.006553	0.066	0.555	45.68	2.79	42.16	0.06	42.10	0.03
z4		0.76	30	0.59	1687	0.24	0.046913	0.264	0.042391	0.282	0.006554	0.041	0.497	44.79	6.30	42.16	0.12	42.11	0.02
AD12	(N 45˚57'35.3"/E 10˚25'56.9")																		
s1		0.07	2.3	59.8	177	0.02	0.046726	0.483	0.041628	0.493	0.006461	0.052	0.238	35.25	11.56	41.41	0.20	41.52	0.02
s2		0.02	5.6	39.7	413	0.01	0.046944	0.261	0.041930	0.281	0.006478	0.079	0.381	46.38	6.23	41.71	0.11	41.62	0.03
s3		0.12	1.8	16.7	140	0.04	0.046849	0.774	0.041835	0.802	0.006476	0.053	0.549	41.54	18.50	41.61	0.33	41.62	0.02
s4		0.19	1.4	25.9	114	0.06	0.047005	0.837	0.041837	0.857	0.006455	0.049	0.437	49.47	19.95	41.62	0.35	41.48	0.02
z2	2.6	0.46	37	1.55	2262	0.15	0.046709	0.185	0.041859	0.204	0.006500	0.061	0.456	34.36	4.42	41.64	0.08	41.76	0.03
z4	4.0	0.65	23	0.99	1349	0.21	0.046846	0.303	0.042029	0.325	0.006507	0.057	0.463	41.39	7.23	41.80	0.13	41.81	0.02
z1	3.6	0.82	21	1.38	1171	0.26	0.046845	0.373	0.042034	0.396	0.006508	0.044	0.572	41.35	8.91	41.81	0.16	41.82	0.02
z6		0.54	27	1.35	1644	0.17	0.046952	0.240	0.042140	0.256	0.006509	0.035	0.510	46.79	5.73	41.91	0.11	41.83	0.01

z7		0.59	4.8	0.92	304	0.19	0.046829	1.520	0.042055	1.611	0.006513	0.120	0.769	40.53	36.33	41.83	0.66	41.85	0.05
z3	4.3	0.73	5.8	1.21	351	0.24	0.046875	1.224	0.042115	1.296	0.006516	0.083	0.878	42.87	29.24	41.89	0.53	41.87	0.03
z8		0.36	24	0.62	1489	0.12	0.048844	0.270	0.054971	0.288	0.008162	0.034	0.569	140.33	6.32	54.34	0.15	52.41	0.02
RdC3																			
s1		11.85	0.3	146.3	29	1.23	0.014924	23.222	0.012167	23.306	0.005913	0.206	0.409	-4192.73	1515.66	12.28	2.84	38.01	0.08
s2		3.63	1.3	119.9	62	1.14	0.045747	2.139	0.040864	2.197	0.006479	0.130	0.467	-15.71	51.71	40.67	0.88	41.63	0.05
s3		3.36	1.6	88.1	75	1.05	0.045872	2.274	0.040934	2.371	0.006472	0.185	0.551	-9.09	54.89	40.74	0.95	41.59	0.08
s4		3.99	0.7	52.4	39	1.31	0.047945	3.404	0.042521	3.447	0.006432	0.105	0.421	96.54	80.58	42.28	1.43	41.33	0.04
s5		3.19	1.1	30.0	58	1.03	0.047038	2.227	0.041939	2.293	0.006466	0.108	0.624	51.18	53.15	41.72	0.94	41.55	0.04
z7		0.76	36	0.62	2078	0.25	0.046829	0.234	0.042096	0.250	0.006520	0.036	0.497	40.53	5.59	41.87	0.10	41.89	0.02
z6		0.74	5.1	0.37	308	0.24	0.046488	1.525	0.041842	1.614	0.006528	0.104	0.867	23.01	36.56	41.62	0.66	41.94	0.04
z8		0.74	5.1	0.42	308	0.24	0.046492	1.511	0.041854	1.600	0.006529	0.105	0.853	23.22	36.24	41.63	0.65	41.95	0.04
z1		0.69	6.4	2.58	388	0.22	0.047106	1.065	0.042465	1.129	0.006538	0.074	0.859	54.62	25.39	42.23	0.47	42.01	0.03
z5		0.68	10	1.17	587	0.22	0.047077	0.724	0.042439	0.767	0.006538	0.056	0.786	53.12	17.25	42.20	0.32	42.01	0.02
z4	1.3	0.74	3.6	1.44	225	0.24	0.047026	1.977	0.042403	2.094	0.006540	0.131	0.900	50.53	47.15	42.17	0.86	42.02	0.05
z2		0.97	1.9	2.05	121	0.32	0.047673	3.866	0.043037	4.097	0.006547	0.242	0.956	83.10	91.67	42.79	1.72	42.07	0.10
z3	2.2	0.72	20	1.04	1134	0.24	0.048569	0.365	0.063043	0.391	0.009414	0.063	0.486	127.09	8.58	62.08	0.24	60.40	0.04

						Radiogenic Isotope Ratios								Isotopic Ages (Ma)					
	Epsilon	Th	Pb*	Pb_c	^{206}Pb	^{208}Pb	^{207}Pb		^{207}Pb		^{206}Pb		corr.	^{207}Pb		^{207}Pb		^{206}Pb	
Sample	Hf(T)	U	Pb_c	(pg)	^{204}Pb	^{206}Pb	^{206}Pb	% err	^{235}U	% err	^{238}U	% err	coef.	^{206}Pb	±	^{235}U	±	^{238}U	±
(a)	(b)	(c)	(e)	(d)	(e)	(f)	(f)	(g)	(f)	(g)	(f)	(g)		(h)	(g)	(h)	(g)	(h)	(g)

(a) z1, z2 etc. are labels for single zircon grains; all zircons annealed and chemically abraded after Mattinson (2005). s1, s2 are sphene fractions.
(b) Epsilon Hf at the time of zircon crystallization. See SOM Table 2 for isotopic data.
(c) Model Th/U ratio calculated from radiogenic 208Pb/206Pb ratio and 207Pb/235U age.
(d) Pb* and Pbc represent radiogenic and common Pb, respectively.
(e) Measured ratio corrected for spike and fractionation only.
(f) Corrected for fractionation, spike, and common Pb, which was assumed to be blank: 206Pb/204Pb = 18.39 ± 0.60%; 207Pb/204Pb = 15.62± 0.66%; 208Pb/204Pb = 37.62 ± 0.78% (all uncertainties 1-sigma). 206Pb/238U and 207Pb/206Pb ratios corrected for initial disequilibrium in 230Th/238U using Th/U [magma] = 4±2.
(g) Errors are 2-sigma, propagated using the algorithms of Schmitz and Schoene (2007) and Crowley et al. (2007).
(h) Calculations are based on the decay constants of Jaffey et al. (1971). 206Pb/238U and 207Pb/206Pb ages corrected for initial disequilibrium in 230Th/238U using Th/U [magma] = 4±2.

Supplementary Table 2: Hf isotopic data

Sample/zircon	$^{176}Hf/^{177}Hf$	± 2σ	$^{176}Hf/^{177}Hf$ (T) (a)	ε Hf (T) (a,b)	±2σ
AD1 z1	0.282896	0.000008	0.282892	**4.7**	**0.3**
AD1 z2	0.282930	0.000006	0.282925	**5.9**	**0.3**
AD1 z3	0.282909	0.000003	0.282905	**5.2**	**0.3**
AD2 z1	0.282942	0.000013	0.282937	**6.3**	**0.3**
AD2 z3	0.282950	0.000007	0.282946	**6.6**	**0.3**
AD2 z4	0.282895	0.000012	0.282891	**4.7**	**0.3**
AD12 z1	0.282937	0.000004	0.282860	**3.6**	**0.3**
AD12 z2	0.282911	0.000003	0.282834	**2.6**	**0.3**
AD12 z3	0.282959	0.000007	0.282881	**4.3**	**0.3**
AD12 z4	0.282949	0.000004	0.282871	**4.0**	**0.3**
AD3 z2	0.282762	0.000029	0.282757	**-0.1**	**0.3**
AD3 z3	0.282805	0.000003	0.282800	**1.5**	**0.3**
AD3 z4	0.282796	0.000005	0.282792	**1.2**	**0.3**
AD3 z5	0.282771	0.000011	0.282767	**0.3**	**0.3**
AD3 z6	0.282831	0.000025	0.282826	**2.4**	**0.3**
AD3 z7	0.282815	0.000017	0.282811	**1.8**	**0.3**
AD3 z9	0.282967	0.000007	0.282890	**4.6**	**0.3**
AD3 z10	0.282912	0.000004	0.282834	**2.7**	**0.3**
AD3 z11	0.283047	0.000004	0.282970	**7.5**	**0.3**
AD5 z1	0.282829	0.000010	0.282825	**2.3**	**0.3**
AD5 z2	0.282811	0.000030	0.282806	**1.7**	**0.3**
AD5 z3	0.282802	0.000004	0.282797	**1.4**	**0.3**
AD5 z4	0.282832	0.000014	0.282828	**2.4**	**0.3**
AD5 z5	0.282777	0.000016	0.282772	**0.5**	**0.3**
AD5 z6	0.282750	0.000037	0.282746	**-0.4**	**0.3**
AD5 z7	0.282752	0.000036	0.282748	**-0.4**	**0.3**
AD5 z9	0.282925	0.000003	0.282847	**3.1**	**0.3**
AD5 z10	0.282881	0.000003	0.282803	**1.6**	**0.3**
AD5 z11	0.282872	0.000011	0.282794	**1.3**	**0.3**
AD7 z1	0.283061	0.000007	0.283057	**10.5**	**0.3**
AD7 z2	0.283046	0.000008	0.283041	**10.0**	**0.3**
AD7 z3	0.283071	0.000003	0.283067	**10.9**	**0.3**
AD7 z5	0.283061	0.000006	0.283057	**10.5**	**0.3**
AD7 z6	0.283105	0.000011	0.283080	**11.4**	**0.3**
RdC3 z3	0.282844	0.000004	0.282819	**2.2**	**0.3**
RdC3 z4	0.282821	0.000009	0.282796	**1.3**	**0.3**

(a) calculated with an esimated 176Lu/177Lu = 0.005 and the 176Lu decay constant of Scherer et al. (2001)

(b) calculated with present day CHUR values of 176Hf/177Hf = 0.282772, 176Lu/177Hf = 0.0332

(c) quoted uncertainties represent reproducibility of standard measurements, which are typically much larger than measurment uncertainties

Supplementary table 3: geochemical data for single zircon and titanite analyses used for geochronology and Hf isotopes

	Epsilon Hf(T) (a)	206Pb/238U date (Ma) (a)	± 2σ	Sc ppm	± 2σ	Y ppm	± 2σ	Zr ‰	± 2σ	Nb ppm	± 2σ	La ppm	± 2σ	Ce ppm	± 2σ	Pr ppm	± 2σ	Nd ppm	± 2σ	Sm ppm	± 2σ	Eu ppm	± 2σ	Gd ppm	± 2σ	Tb ppm	± 2σ	Dy ppm	± 2σ	Ho ppm	± 2σ	Er ppm	± 2σ	Tm ppm	± 2σ	Yb ppm	± 2σ	Lu ppm	± 2σ	Hf ‰	± 2σ	Ta ppm	± 2σ	Th ppm	± 2σ
Zircon: Zr+Hf-normalized (b,c)																																													
AD1 z5		42.06	0.02	350.5	11.7	680.9	16.9	488.4	14.0	6.9	1.6	-0.1	0.1	26.2	2.5	0.0	0.1	0.1	0.3	0.7	0.5	0.7	0.3	7.6	2.1	3.0	0.8	32.0	1.8	16.3	0.7	95.6	5.5	26.8	0.6	323.0	20.3	96.6	5.5	9.1	0.2	0.3	0.2	3433.2	129.4
AD1 z6		42.08	0.02	344.7	8.6	645.6	15.4	488.3	9.8	4.2	1.2	0.0	0.1	16.4	1.2	0.1	0.1	0.6	0.4	1.0	0.7	0.5	0.3	5.2	0.9	2.1	0.3	32.4	2.9	15.7	1.0	95.1	3.9	26.4	1.7	302.9	14.7	87.3	1.5	9.4	0.1	0.2	0.1	1945.3	45.8
AD1 z7		42.24	0.06	326.5	3.8	420.0	5.7	489.6	4.1	5.0	0.8	0.1	0.1	9.4	0.8	0.1	0.0	0.6	0.3	0.6	0.4	0.6	0.2	4.1	0.7	1.7	0.3	23.6	1.8	10.7	0.8	64.5	2.3	16.8	0.8	179.0	5.8	44.4	2.1	8.2	0.2	0.4	0.1	205.0	5.6
AD1 z8		42.11	0.02	363.5	10.8	722.9	16.2	487.9	10.6	3.5	1.1	0.1	0.1	16.7	1.0	0.1	0.1	0.2	0.3	0.9	0.9	0.6	0.3	5.4	1.5	2.5	0.2	35.5	3.7	17.6	1.6	108.2	7.1	29.2	1.1	330.5	7.9	96.4	0.9	9.5	0.3	0.1	0.2	1873.5	18.0
AD2 z5		42.09	0.02	320.4	2.9	2371.6	62.5	490.4	13.6	7.2	0.5	0.8	0.1	55.7	2.3	0.6	0.0	5.2	0.4	7.2	1.3	3.8	0.3	37.8	1.6	13.9	0.4	159.6	6.2	64.5	1.1	330.1	10.4	74.7	2.3	719.9	13.4	159.7	4.3	7.1	0.2	0.8	0.1	3730.1	99.2
AD2 z6		42.09	0.02	321.3	10.6	416.2	7.7	490.4	8.9	3.7	0.7	0.1	0.1	8.8	0.6	0.1	0.1	0.6	0.2	0.8	0.4	0.5	0.2	4.4	0.9	1.6	0.1	21.6	0.9	10.5	0.5	61.9	2.4	16.2	1.1	185.4	5.2	47.9	1.9	7.1	0.2	0.3	0.1	321.8	9.4
AD2 z7		42.08	0.02	329.0	11.0	576.7	14.5	490.3	11.7	3.8	0.8	0.0	0.1	17.4	1.5	0.1	0.0	0.6	0.3	1.3	0.3	0.9	0.3	6.2	1.0	2.6	0.2	32.6	1.5	14.3	0.9	81.9	1.7	21.2	0.9	233.2	9.0	55.5	1.8	7.3	0.1	0.4	0.1	1307.3	21.3
AD2 z8		42.08	0.02	341.9	14.6	1927.6	59.8	490.1	16.9	8.1	0.9	0.1	0.1	45.0	2.4	0.3	0.1	2.9	1.2	5.5	0.9	3.4	0.8	31.2	0.8	10.8	0.8	123.9	2.8	50.5	2.1	262.6	11.5	62.5	3.0	621.2	25.4	139.4	5.3	7.5	0.2	0.9	0.1	5431.1	156.7
AD3 z9	4.6	41.98	0.03	374.8	11.5	832.3	8.6	486.2	9.2	8.1	2.1	0.4	0.4	18.6	2.0	0.2	0.1	1.6	0.8	1.2	0.7	0.4	0.6	11.1	2.2	4.0	0.5	50.2	5.6	20.0	2.1	119.4	11.4	28.8	0.9	300.9	9.4	74.2	2.5	11.3	0.3	1.3	0.4	330.1	15.2
AD3 z10	2.7	42.00	0.02	346.5	11.7	804.5	16.3	488.0	13.0	6.8	1.5	0.1	0.1	18.2	1.0	0.1	0.1	1.0	0.7	2.1	0.7	0.8	0.2	10.4	1.2	3.8	0.2	45.6	2.4	20.7	0.6	117.8	3.8	27.7	0.8	287.4	8.2	67.7	2.9	9.6	0.4	0.9	0.1	327.8	9.8
AD3 z8		42.06	0.05	396.8	46.9	872.1	33.6	487.7	13.4	1.7	2.6	0.3	1.1	20.0	2.3	-0.2	0.6	0.8	1.8	4.6	1.1	0.6	0.2	14.1	4.1	4.5	0.6	54.6	10.5	26.0	2.5	125.1	3.1	26.1	2.5	294.0	28.4	76.6	6.0	10.0	0.2	-0.3	2.9	287.5	12.3
AD3 z11	7.5	42.08	0.03	324.0	4.0	558.1	16.2	487.7	7.1	5.2	0.5	0.2	0.2	12.6	0.7	0.1	0.0	0.8	0.5	1.8	0.6	0.6	0.2	7.0	1.0	2.7	0.3	33.5	2.8	15.2	0.7	83.1	5.0	21.3	1.0	223.8	14.9	54.6	0.6	9.7	0.3	0.7	0.2	212.0	9.3
AD3 z3	1.5	42.90	0.01	350.2	18.1	718.6	21.9	488.8	9.6	2.0	0.5	1.2	0.2	17.2	1.0	0.3	0.1	2.8	0.6	1.8	0.3	0.6	0.1	10.4	0.8	3.5	0.4	41.6	3.0	20.3	1.4	107.1	8.0	22.3	1.0	244.7	10.1	62.0	3.0	8.2	0.4	0.6	0.5	208.3	1.4
AD5 z11	1.3	41.85	0.06	383.2	13.1	1135.0	31.7	486.4	16.7	6.1	1.7	1.4	0.4	28.0	2.9	0.5	0.2	3.5	1.7	4.5	1.4	1.2	0.7	19.4	4.7	5.9	0.6	77.1	3.2	29.6	4.3	153.6	6.6	38.0	3.8	367.6	10.8	83.8	5.6	11.2	0.3	1.2	0.4	472.0	18.0
AD5 z9	3.1	41.91	0.02	335.1	11.8	954.8	24.6	487.5	7.5	6.9	0.6	0.5	0.1	24.5	1.7	0.2	0.1	0.9	0.4	2.5	0.9	0.9	0.2	11.6	1.1	4.1	0.2	54.3	3.1	24.2	0.4	135.9	4.1	33.5	1.4	345.3	11.2	81.2	3.2	9.9	0.2	0.6	0.2	457.8	15.2
AD5 z2	10	41.93	0.05	424.2	65.4	813.4	28.6	488.2	7.9	0.1	4.0	2.3	2.2	17.5	4.6	0.3	0.9	1.1	2.5	0.7	1.4	0.5	0.4	13.0	7.1	3.2	0.6	44.0	1.2	19.5	2.7	106.1	11.0	27.0	2.0	274.3	5.1	69.3	5.1	9.6	0.4	3.0	4.7	198.1	5.7
AD5 z10	1.6	41.99	0.02	336.3	7.9	567.8	10.5	487.9	7.5	5.1	0.6	1.6	0.3	16.7	0.7	0.4	0.1	1.5	0.3	1.7	0.4	0.5	0.2	7.8	1.3	2.9	0.4	33.7	1.3	14.7	0.7	82.3	2.2	20.2	0.6	206.8	12.3	48.7	2.1	9.6	0.1	1.2	0.2	187.2	4.1
AD5 z3	1.4	42.00	0.02	367.1	21.1	736.3	13.4	489.0	12.1	2.3	0.7	0.5	0.2	16.3	0.7	0.2	0.1	1.5	0.6	1.9	0.6	0.5	0.2	9.8	0.8	3.5	0.2	47.1	0.8	20.7	1.0	110.8	5.0	23.8	0.9	249.3	15.9	58.8	2.2	8.6	0.3	0.6	0.7	181.2	12.0
AD5 z8		42.01	0.11	358.9	126.4	966.6	50.0	487.9	9.3	-1.8	8.0	-0.4	3.8	19.3	7.7	-0.3	1.8	0.1	5.7	6.8	5.8	1.4	0.8	11.8	7.8	5.0	0.9	57.4	7.9	32.7	2.9	136.2	7.0	32.5	1.1	266.2	42.7	70.2	3.3	9.6	0.6	-4.0	9.3	365.8	6.9
RdC3 z7		41.89	0.02	313.6	6.0	697.4	17.2	487.8	9.7	5.0	0.6	1.4	0.2	19.0	0.9	0.3	0.1	1.5	0.4	2.7	0.4	1.0	0.2	9.9	0.7	3.5	0.4	42.1	1.7	18.2	0.3	102.2	4.8	25.6	0.9	255.8	9.5	62.9	1.5	9.9	0.2	0.6	0.1	298.9	2.9
RdC3 z6		41.94	0.04	319.2	5.0	639.3	16.9	488.5	6.6	5.3	0.5	0.9	0.2	15.4	0.6	0.2	0.1	1.4	0.3	2.0	0.4	0.8	0.2	8.4	0.9	3.2	0.1	39.9	1.3	17.2	0.8	94.6	2.2	23.0	0.6	225.9	5.5	52.7	1.5	9.0	0.2	0.6	0.1	200.4	4.3
RdC3 z8		41.95	0.04	372.5	8.6	815.1	18.8	486.0	6.6	13.5	2.8	0.4	0.4	19.1	2.3	0.2	0.2	1.7	1.0	2.6	1.1	1.0	1.3	10.4	3.3	4.2	0.9	49.6	4.7	22.3	3.0	120.0	2.7	29.3	2.2	294.1	20.7	67.3	3.2	11.6	0.2	0.9	0.6	330.8	8.8
RdC3 z1		42.01	0.03	333.4	11.8	674.7	20.9	489.0	8.1	1.7	0.6	0.4	0.3	16.4	0.6	0.1	0.1	1.2	0.5	1.7	0.4	0.8	0.1	9.3	1.0	3.4	0.0	43.4	3.2	19.4	0.7	96.7	0.6	22.3	0.6	232.0	15.1	58.0	1.8	8.8	0.2	0.5	0.7	202.4	12.8
RdC3 z5		42.01	0.02	345.1	14.6	711.4	25.2	487.9	5.8	2.0	1.0	0.0	0.4	16.8	1.1	0.0	0.2	0.7	0.8	1.9	0.5	0.8	0.1	8.9	0.6	3.6	0.4	45.5	1.1	20.5	1.7	107.9	5.2	23.9	0.9	252.2	22.5	64.2	2.8	9.5	0.5	0.4	1.0	251.8	8.5
RdC3 z4	1.3	42.02	0.05	359.4	24.1	598.2	19.8	488.1	27.3	1.2	1.4	1.8	0.7	18.4	1.4	0.5	0.3	1.0	0.9	2.1	0.4	0.5	0.1	8.9	2.2	2.7	0.6	38.4	3.6	18.9	1.9	88.1	2.3	19.7	1.7	215.8	16.5	52.2	2.9	9.1	0.4	0.0	1.6	195.2	6.7
RdC3 z2		42.07	0.10	376.8	41.0	832.5	27.9	488.0	14.4	1.0	2.7	-0.7	1.2	19.3	3.1	0.1	0.6	1.0	2.1	4.6	1.3	0.8	0.6	17.4	5.6	5.0	0.8	54.1	0.7	23.4	0.7	125.7	6.1	25.9	1.2	276.8	7.9	68.2	2.6	10.0	0.1	-0.6	3.0	310.0	9.8
RdC3 z3	2.2	60.40	0.04	337.5	13.3	560.3	5.4	488.7	16.8	1.9	0.6	-0.1	0.3	12.9	0.9	0.0	0.1	0.6	0.3	2.1	0.8	0.4	0.1	8.9	0.4	2.5	0.2	37.1	1.2	16.9	1.1	87.3	1.2	19.8	1.5	198.0	19.1	50.2	1.7	9.0	0.6	0.4	0.7	164.6	9.0
AD7 z5	10.5	42.06	0.02	355.0	18.8	274.9	13.1	490.3	34.6	0.7	0.9	0.2	0.4	5.4	1.0	0.0	0.2	0.6	0.7	0.9	0.8	0.6	0.1	2.5	1.8	0.9	0.2	15.2	0.8	7.3	0.9	36.6	3.6	10.4	0.7	118.1	3.9	32.9	1.2	7.5	0.1	-0.1	1.0	85.8	2.8
AD7 z2	10	42.07	0.02	373.0	43.5	460.9	29.8	489.4	29.0	0.1	2.5	-0.1	1.2	7.5	2.4	0.0	0.6	0.8	1.7	2.6	0.5	0.5	0.3	4.6	1.5	1.8	0.2	22.2	2.7	11.8	0.7	65.0	1.2	16.2	2.2	194.7	10.0	53.3	4.9	8.1	0.2	7.0	3.0	147.7	3.2
AD7 z6	11.4	42.09	0.02	332.8	12.8	333.7	7.5	490.7	12.1	0.7	0.7	-0.1	0.3	6.4	0.7	0.0	0.2	0.3	0.5	1.0	0.4	0.5	0.1	4.2	0.6	1.5	0.3	16.9	1.0	8.9	0.3	50.7	2.9	13.5	0.7	148.9	11.7	44.3	2.3	7.1	0.4	0.0	0.7	103.5	5.6
AD7 z1	10.5	42.10	0.03	336.5	15.5	354.8	11.1	490.5	29.4	6.8	0.8	11.9	0.7	27.7	0.8	2.1	0.2	8.3	0.7	2.6	0.4	0.7	0.3	4.7	0.6	1.5	0.1	20.1	2.4	9.4	0.8	54.2	3.2	14.1	1.2	162.9	7.5	47.7	3.2	7.0	0.3	2.0	0.8	141.7	2.2
AD7 z3	10.9	42.10	0.03	325.6	12.1	391.8	10.2	490.3	14.8	1.9	0.5	0.2	0.2	8.4	0.5	0.0	0.1	0.5	0.4	0.9	0.1	0.5	0.1	4.6	1.2	1.5	0.0	20.9	2.3	10.6	0.4	55.2	0.4	13.1	0.6	176.8	4.0	48.9	2.7	7.5	0.0	2.0	0.5	170.3	9.6
AD7 z4		42.11	0.02	361.6	25.8	509.8	20.3	490.0	22.6	0.6	1.2	-0.1	0.6	7.1	1.2	0.0	0.3	0.6	0.8	2.0	1.0	1.2	0.6	7.4	1.9	2.6	0.3	30.2	1.7	12.8	0.7	70.8	6.6	17.3	0.7	208.6	11.9	56.6	2.1	7.5	0.3	0.4	1.4	162.0	6.7
AD12 z2	2.6	41.76	0.03	360.1	11.1	1010.6	18.6	488.9	8.1	2.9	0.3	-0.1	0.1	13.0	0.4	0.0	0.1	0.5	0.3	2.0	0.3	0.8	0.2	12.0	0.5	4.9	0.1	67.8	1.1	30.6	0.8	152.5	1.2	33.8	0.8	337.6	2.5	80.1	2.5	8.6	0.3	1.0	0.3	215.7	5.8
AD12 z4	4	41.81	0.02	340.0	11.5	751.4	23.0	489.9	23.2	2.6	0.8	-0.3	0.3	17.1	1.1	0.0	0.1	0.8	0.5	2.2	1.1	0.6	0.1	12.1	1.4	3.3	0.2	47.6	3.5	20.1	0.5	103.6	5.4	23.6	1.4	247.9	12.1	58.1	3.8	7.8	0.3	0.6	0.8	271.6	4.8
AD12 z1	3.6	41.82	0.02	363.6	24.6	662.7	66.4	489.3	17.7	1.9	0.9	0.1	0.4	17.1	0.8	0.1	0.2	1.3	1.0	2.6	0.5	0.9	0.3	10.7	0.7	3.7	0.4	45.2	6.0	19.7	1.6	94.4	4.2	23.0	1.3	231.8	11.3	56.7	5.4	8.6	0.6	0.5	0.9	350.8	22.4
AD12 z6		41.83	0.01	341.0	11.5	955.2	38.7	487.7	19.1	8.1	0.7	0.2	0.1	18.6	0.4	0.2	0.0	1.7	0.3	3.9	0.5	1.4	0.3	15.0	1.0	5.6	0.6	64.7	2.1	25.9	0.7	135.9	2.1	32.5	0.7	326.3	16.3	75.0	2.5	10.0	0.3	0.7	0.1	320.2	10.1
AD12 z7		41.85	0.05	390.3	15.7	851.4	26.3	486.6	11.8	7.2	1.4	0.4	0.3	17.1	2.3	0.1	0.1	0.6	0.4	1.8	1.2	1.0	0.4	10.8	2.2	4.6	0.8	56.2	3.6	23.8	1.9	118.6	6.2	31.2	2.1	284.1	10.6	69.0	2.2	11.0	0.3	1.3	0.5	310.2	16.2
AD12 z3	4.3	41.87	0.03	401.1	30.8	684.1	30.3	488.3	3.0	1.7	1.9	-0.3	0.9	17.4	2.5	-0.1	0.4	0.8	1.8	2.5	0.8	0.8	0.2	9.3	2.4	3.4	0.8	40.8	1.9	18.3	2.7	90.4	3.2	22.2	1.7	232.9	12.1	58.9	2.4	9.4	0.3	-0.3	2.3	275.6	5.9
AD12 z8		52.41	0.02	358.6	10.9	637.1	23.5	486.9	17.4	7.1	1.1	0.2	0.1	16.0	1.8	0.1	0.1	0.6	0.4	1.2	0.7	0.5	0.3	7.0	1.9	3.1	0.7	35.9	2.5	15.9	1.3	86.7	1.9	23.7	1.7	239.0	9.6	60.8	2.3	10.5	0.3	1.3	0.4	340.8	4.4
Titanite: not Zr+Hf-normalized (b,c)				ppt	± 2σ	ppt	± 2σ	ppb	± 2σ	ppb	± 2σ	ppb	± 2σ	ppb	± 2σ	ppb	± 2σ	ppb	± 2σ	ppb	± 2σ	ppb	± 2σ	ppb	± 2σ	ppb	± 2σ	ppb	± 2σ	ppb	± 2σ	ppb	± 2σ	ppb	± 2σ	ppb	± 2σ	ppb	± 2σ	ppb	± 2σ	ppb	± 2σ	ppb	± 2σ
AD3 s1		41.99	0.02	-	-	72.83	4.49	11.04	0.19	43.28	2.91	16.34	0.52	73.50	1.40	11.81	0.50	55.31	0.49	12.20	0.40	2.47	0.07	11.81	0.66	1.79	0.05	11.16	0.45	2.43	0.07	6.80	0.08	1.03	0.05	7.01	0.23	0.97	0.01	1.34	0.06	5.422	0.055	18.38	1.18
AD3 s2		42.01	0.02	-	-	65.70	5.34	10.51	1.30	42.70	3.13	15.97	1.15	67.43	3.02	10.19	0.28	46.71	1.37	10.34	0.31	2.10	0.08	10.27	0.74	1.52	0.11	9.27	0.67	2.01	0.18	5.88	0.37	0.85	0.06	6.56	0.52	0.95	0.11	1.15	0.06	4.089	0.296	19.16	1.59
AD3 s3		42.12	0.05	-	-	97.30	6.98	12.14	0.99	64.50	3.11	20.10	1.86	99.32	10.02	15.95	1.05	77.43	7.00	17.44	1.88	3.61	0.36	16.58	1.79	2.47	0.18	14.55	1.10	3.28	0.35	9.20	0.84	1.34	0.18	8.81	0.67	1.25	0.09	1.33	0.09	9.793	0.647	21.63	1.13
AD5 s1		41.25	0.02	-	-	29.96	0.79	7.12	0.40	22.06	0.75	19.31	0.41	72.58	3.27	10.64	0.58	45.10	0.80	8.11	0.09	2.43	0.04	6.30	0.09	0.85	0.05	4.73	0.21	1.01	0.07	2.95	0.14	0.44	0.02	3.28	0.26	0.50	0.01	0.58	0.02	4.040	0.220	14.96	0.92
AD5 s2		41.12	0.03	-	-	17.02	0.93	5.01	0.31	18.32	0.61	14.85	0.75	45.26	0.49	5.89	0.28	23.18	0.89	3.91	0.03	1.62	0.03	3.14	0.10	0.40	0.02	2.36	0.15	0.52	0.03	1.61	0.12	0.24	0.01	1.84	0.03	0.29	0.01	0.34	0.02	1.588	0.022	10.02	0.28
AD5 s3		41.10	0.02	-	-	22.42	1.82	8.96	0.75	27.56	1.34	19.83	1.05	62.17	6.03	7.44	0.77	30.24	1.98	4.84	0.64	2.49	0.19	3.97	0.15	0.53	0.05	3.11	0.12	0.69	0.06	2.11	0.19	0.32	0.03	2.39	0.12	0.39	0.01	0.50	0.03	1.425	0.050	11.40	0.69
AD7 s1		42.10	0.16	-	-	5.04	0.48	2.76	0.55	3.57	0.24	5.40	0.39	16.36	1.99	1.98	0.22	7.76	0.88	1.30	0.14	0.39	0.03	1.03	0.10	0.13	0.01	0.82	0.13	0.18	0.03	0.49	0.06	0.07	0.00	0.53	0.08	0.07	0.01	0.15	0.03	0.191	0.022	2.17	0.14
AD7 s2		42.05	0.09	-	-	4.46	0.18	2.54	0.20	2.26	0.02	7.07	0.19	17.67	0.25	1.95	0.03	7.11	0.21	1.04	0.07	0.35	0.02	0.92	0.10	0.12	0.00	0.66	0.03	0.15	0.01	0.43	0.02	0.05	0.00	0.42	0.02	0.07	0.00	0.15	0.01	0.015	0.004	3.87	0.06
AD7 s3		41.10	0.02	-	-	4.66	0.36	2.33	0.24	1.73	0.10	5.43	0.13	15.06	0.63	1.66	0.07	6.36	0.14	1.04	0.08	0.34	0.01	0.89	0.07	0.12	0.01	0.69	0.02	0.16	0.01	0.44	0.03	0.07	0.01	0.49	0.04	0.08	0.01	0.18	0.02	0.018	0.004	2.85	0.08
AD12 s1		41.58	0.02	73.76	5.55	127.44	2.40	7.44	0.87	107.37	2.13	10.83	0.16	61.43	1.70	13.04	0.36	67.47	0.99	20.78	0.71	6.83	0.16	19.26	0.44	3.27	0.06	18.13	0.27	3.73	0.04	11.07	0.25	1.67	0.04	11.12	0.21	1.49	0.03	1.12	0.06	3.670	0.084	2.17	0.05
AD12 s2		41.65	0.03	48.77	2.89	47.04	0.52	8.68	0.84	42.23	0.31	6.70	0.09	33.51	0.29	6.25	0.05	29.26	0.36	7.61	0.06	3.97	0.09	6.82	0.17	1.11	0.03	6.16	0.10	1.31	0.02	4.13	0.05	0.67	0.01	4.81	0.08	0.71	0.02	0.63	0.03	0.888	0.010	0.83	0.03
AD12 s3		41.69	0.03	21.13	1.85	9.92	0.13	1.80	0.84	8.37	0.18	5.50	0.08	18.34	0.16	2.59	0.04	10.13	0.16	2.01	0.05	0.90	0.02	1.60	0.03	0.25	0.01	1.35	0.03	0.28	0.01	0.86	0.03	0.14	0.00	0.95	0.03	0.14	0.00	0.14	0.01	0.053	0.002	0.86	0.02
AD12 s4		41.58	0.02	148.99	5.64	27.26	0.48	3.48	0.85	30.24	0.12	7.52	0.11	29.51	0.37	4.80	0.05	20.97	0.31	5.06	0.07	1.96	0.04	4.54	0.10	0.74	0.02	4.05	0.12	0.84	0.01	2.54	0.05	0.38	0.01	2.53	0.04	0.35	0.01	0.31	0.03	0.641	0.013	1.56	0.02
AD12 s5				14.76	2.09	10.30	0.17	1.65	0.84	23.10	0.23	1.83	0.03	8.86	0.08	1.57	0.02	7.06	0.12	1.74	0.03	0.89	0.02	1.52	0.03	0.25	0.01	1.35	0.04	0.29	0.01	0.91	0.01	0.14	0.01	1.06	0.02	0.16	0.01	0.14	0.03	0.391	0.009	0.57	0.01
RdC3 s1		38.92	0.08	75.77	4.44	49.33	1.00	8.65	0.86	53.78	0.99	16.88	0.28	68.73	1.60	10.38	0.20	42.06	0.90	9.30	0.23	1.99	0.04	8.01	0.11	1.26	0.03	6.88	0.16	1.47	0.03	4.50	0.06	0.68	0.01	4.63	0.15	0.64	0.02	1.06	0.03	2.282	0.028	22.96	0.58
RdC3 s2		41.86	0.05	214.91	7.16	159.96	3.18	24.61	0.97	221.21	4.03	48.47	1.07	201.15	2.91	28.95	0.59	121.18	2.66	27.29	0.33	5.70	0.13	24.35	0.63	3.87	0.09	21.04	0.56	4.37	0.09	13.29	0.25	1.98	0.04	13.51	0.36	1.86	0.03	2.99	0.07	9.138	0.149	65.32	1.15
RdC3 s3		41.76	0.08	180.43	5.20	138.02	1.19	19.90	0.97	229.45	7.11	40.10	0.19	169.41	1.50	25.04	0.29	105.01	1.58	24.00	0.41	5.05	0.05	21.25	0.19	3.38	0.07	18.40	0.24	3.81	0.06	11.54	0.06	1.73	0.02	11.72	0.18	1.59	0.03	2.55	0.07	7.205	0.096	54.03	0.75
RdC3 s4		41.80	0.05	60.18	1.99	31.08	1.02	5.79	0.86	52.54	1.04	11.57	0.28	43.36	0.97	6.52	0.18	26.55	0.64	5.88	0.15	1.22	0.03	5.25	0.22	0.82	0.03	4.51	0.17	0.94	0.04	2.87	0.05	0.43	0.01	2.92	0.09	0.41	0.01	0.71	0.03	1.694	0.043	14.80	0.25
RdC3 s5		41.79	0.05	47.72	4.12	26.31	0.29	4.48	0.85	25.10	0.26	9.76	0.09	35.98	0.21	5.34	0.05	21.67	0.27	4.74	0.04	1.05	0.02	4.30	0.06	0.68	0.01	3.75	0.05	0.79	0.02	2.42	0.05	0.36	0.01	2.58	0.03	0.37	0.01	0.61	0.02	0.464	0.007	13.24	0.15
blank measurements				0.33	1.49	3.95	0.93	4.29	0.92	0.03	1.42	0.05	0.25	-2.71	1.52	-0.24	0.08	0.98	0.36	0.21	0.24	0.42	0.40	-0.20	0.40	-0.04	0.05	0.82	0.19	0.22	0.05	-0.06	0.16	-0.12	0.05	-0.55	0.21	0.12	0.02	-0.05	0.01	0.31	0.32	0.74	0.28

average (n=15; units are in ppt, except for Zr and Hf, which are in ppb. Negative values indicate a slight deviation between the standard calibration curve and blank value - see Schoene et al., 2010)

(a) U-Pb dates are from Table 1. Epsilon Hf(T) are from Table 2; 2-sigma uncertainties are ±0.3 epsilon units.
(b) normalized to Zr+Hf = 497464 ppm in stoichiometric zircon. Unnormalized data at bottom of table are presented as concentrations in measured solutions.
(c) all data are corrected using the blanks and 2SD values given at the bottom of the table. Uncertainties are propagated according to standard error propagation techniques.
(d) "-" indicates that the data was at or below the limits of detection, given the magnitude of the blank correction

SOM.1 ROCK AND ACCESSORY MINERAL DESCRIPTIONS

Two samples from pegmatitic segregations of the Blumone gabbro (AD1, AD2; Fig. SOM 1A-C) were collected. Latitude and longitude (WGS84) are: N 45°57'30.1''/E 10°27'29.5" for AD1 and N45°57'33.9"/E 10°27'27.6" for AD2. These contain coarse-grained plagioclase, acicular and partly skeletal amphibole and potassium feldspar (often overgrowing plagioclase; Fig. SOM1A,B). Late crystallization of chlorite, titanite and clinozoisite make up ~10% of the rock. Zircon can be seen as inclusions in most phases. Cathodoluminescence (CL) imaging of zircon reveals oscillatory and sector zoning with no observed cores or overgrowths, though the sector zoning often occurs at unusual orientations with respect to the oscillatory zoning (Fig. SOM2A,B). CL images also reveal that most of the zircon separates (50-200 μm in diameter) are in fact grain fragments rather than whole grains.

Sample AD7 (N 45°57'51.0"/E 10°26'28.6") comes from what John and Blundy (1993) term the low-K marginal unit of the Vacca tonalite (colloquially called the "spotty dog"). It is characterized by hornblende-rich quartz diorite and tonalite (Fig. SOM1D). Our sample is a quartz diorite and contains abundant (~20 % modal) 3-7 mm hornblende phenocrysts which contain inclusions of ~An50 plagioclase (as determined petrographically) and apatite. Matrix minerals include plagioclase averaging An40, <3 mm hornblende phenocrysts, minor quartz, and titanite. Zircon is located both in the matrix and as inclusions in large amphibole phenocrysts. Zircon from AD7 are euhedral and prismatic and vary from stubby to elongate; grain size ranges from 50-500 μm in length, but are typically 200-400 μm. CL imaging shows oscillatory zoning typical of

igneous zircon, though most of the grains have one or more subtle, rounded cores with truncated oscillatory or sector zoning (Fig. SOM2B), likely reflecting multiple phases of growth and resorption.

Samples AD3 (N 45°57'53.9"/E 10°27'6.8") and AD5 (N 45°57'18.0"/E 10°24'27.0") were collected from the main unit of the Vacca tonalite, and one additional sample (RdC3) is the same sample analyzed in Hansmann and Oberli (1991; Fig SOM1E-G). Our two samples are hornblende biotite tonalites and nearly are indistinguishable in hand sample and thin section, though AD5 has minor potassium feldspar. Both samples have late stage chlorite, epidote, clinozoisite and sericite alteration of plagioclase. Zircon, apatite and titanite were observed petrographically and appear igneous in origin, with the exception of titanite in AD5, which in places is associated with chlorite and epidote, possibly indicating late stage growth. Zircon from AD3 and AD5 are euhedral, 50-200 μm in length and vary from stubby to elongate and prismatic. CL imaging of zircon from both samples reveal distinct oscillatory zoning, and resorbed igneous cores with truncated zonation are observed in both samples, but are far more common in AD5 (Fig. SOM2A). AD3 also commonly has sector zonation in addition to oscillatory zonation.

The Galliner granodiorite (AD12; N 45°57' 35.3"/E 10°25'56.9") is distinguished from the Vacca tonalite by coarser biotite phenocrysts, a less-pronounced magmatic fabric and more potassium feldspar (though the latter is difficult to distinguish in hand sample; Fig. SOM1H). It also contains abundant zircon, titanite and apatite. Zircon are 30-200 μm in length and show similar morphology and textures to the Vacca tonalite samples.

SOM.2 METHODOLOGY

SOM.2.1 U-Pb methodology

Hand samples were processed at the University of Geneva (UNIGE) by first crushing in a standard rock crusher placed in a tungsten mill shatterbox for five second increments and sieved to <500 μm. Separated material was then passed over a Wilfley table prior to magnetic and heavy liquid separation. Single zircons were picked for chemical abrasion (Mattinson, 2005) and combined in a quartz beaker for annealing at 900 ˚C for ~60 hours. All grains from a single sample were leached together in 3 ml savillex beakers in HF + trace HNO_3 for ~12 hours, rinsed with water and acetone and then placed in 6N HCl on a hotplate at ~110 ˚C overnight. These were then washed several times with water, HCl, and HNO_3. Single grains were then handpicked for dissolution. Each grain was spiked with ~0.004 g of the EARTHTIME ($\pm^{202}$Pb)-^{205}Pb-^{233}U-^{235}U tracer solution. Zircons were dissolved in ~70 μl 40% HF and trace HNO_3 in 200 μl savillex capsules at 210 ˚C for 48+ hours, dried down and redissolved in 6N HCl overnight. Samples were then dried down and redissolved in 3N HCl and put through a modified single 50 μl column anion exchange chemistry (Krogh, 1973). Titanite were hand-picked and dissolved in HF + HNO_3 in 3 ml savillex beakers at 140 ˚C on a hotplate for ~ 1 week. They were then converted to 6 N HCl for several days, sonicated, and then dried to salts. The residue was redissolved in HBr and U and Pb were separated by a two-stage HBr-HCl chemistry in 50 μl columns with AGX resin. Zircon and titanite "washes" – the eluted portion not containing U and Pb – were collected for TIMS-TEA and Hf isotope analysis (Schoene et

al., 2010b). U and Pb were collected in the same beaker for zircon and dried down with a drop of 0.05 M H_3PO_4, and analyzed on a single outgassed Re filament in a Si-gel emitter, modified from (Gerstenberger and Haase, 1997). U and Pb were collected and measured separately for titanite. Measurements were performed on a Thermo-Finigan Triton thermal ionization mass spectrometer at the University of Geneva.

Pb was measured in dynamic mode on a modified Masscom secondary electron multiplier (SEM). Deadtime for the SEM was determined by periodic measurement of NBS-982 for up to 1.3 Mcps and observed to be constant at 23.5 ns. Multiplier linearity was monitored every few days between $1.3x10^6$ and <100 cps by a combination of measurements of NBS-981, -982 and -983, and observed to be constant if the Faraday to SEM yield was kept between ~93-94% by adjusting SEM voltage. Baseline measurements were made at masses 203.5 and 204.5 and the average was subtracted from each peak after beam decay correction. Interferences on ^{202}Pb and ^{205}Pb were monitored by measuring masses 201 and 203 and also by monitoring masses 202 and 205 in unspiked samples. As a result, no corrections were applied. Mass fractionation was corrected using the EARTHTIME ^{202}Pb-^{205}Pb-^{233}U-^{235}U tracer, and each measured ratio was corrected for fractionation in the data acquisition software using a $^{202}Pb/^{205}Pb$ of 0.99989, giving an average Pb fractionation of 0.13±0.04 %/a.m.u. (2-sigma standard deviation).

U was measured in static mode on Faraday cups and 10^{12} ohm resistors as UO_2^+. Oxygen isotopic composition was monitored by measurement of mass 272 on large U500 loads (Wasserburg et al., 1981). Though the $^{18}O/^{16}O$ typically grew from 0.00200 to 0.00208 over the course of an analysis, the most drastic increase occurred at the

beginning towards an average value of ~0.00205. As a result, early blocks of data were deleted and the average value was used for all data, and corrected during mass spectrometry. Baselines were measurement at ±0.5 mass units for 30 seconds every 50 ratios. Correction for mass-fractionation for U was done with the double spike assuming a sample $^{238}U/^{235}U$ ratio of 137.88. Measured ratios were reduced using the algorithms of Schmitz and Schoene (2007) and Crowley et al. (2007) (Table 1) using a $^{235}U/^{205}Pb$ = 100.20 for the EARTHTIME ^{202}Pb-^{205}Pb-^{233}U-^{235}U tracer to which a total uncertainty of 0.1 was assigned. Please see Schoene et al. (2010a) for details on the spike composition used and also for discussion of interlaboratory calibration of the zircon standard NMB-03-1; the intercalibration data measured for that study was done over the same time period as this study. All uncertainties in this study are 2-sigma and include internal sources of uncertainty only. External, or systematic, sources of uncertainty such as the tracer composition used and the uranium decay constants should be included when comparing these data to those using another tracer or decay scheme, respectively (see Schoene et al., 2006 for details).

Over 40 total procedural blanks were measured over the course of this study, spiked with the same tracer as samples. The amount of common Pb in blanks agreed well with that found in zircon analyses, suggesting all common Pb came from blank. After 2-sigma outlier rejection, the composition of 27 ^{202}Pb-^{205}Pb-^{233}U-^{235}U -spiked blanks was: $^{206}Pb/^{204}Pb$ = 18.39±0.22, $^{207}Pb/^{204}Pb$ = 15.62±0.20, $^{208}Pb/^{204}Pb$ = 37.62±0.78 (2-sigma standard deviations). Following five total procedural blank analyses for titanite chemistry, a total of 1 pg Pb was applied to the samples with same composition used for zircon. To test the accuracy of the ^{202}Pb-^{205}Pb-^{233}U-^{235}U composition, (Schoene et al.,

2010a) intentionally picked very small fragments (<20 μm diameter) of North Mtn. Basalt (NMB-03-1) in order to achieve a range of ratios of radiogenic Pb to blank Pb, providing a test of the accuracy of the blank correction. Because this did not introduce scatter into their results, we conclude the blank composition is approximately correct, and not the cause of the range in dates seen in samples from this study.

Five total procedural blanks were measured for titanite. The composition agreed very well with zircon blanks, so the analyses were pooled to arrive at the means and SD shown above. The magnitude of the blank was higher, giving an average of 1.5±0.75 pg (2SD), and this value was used to reduce all titanite. Excess common Pb (Pb_c) was attributed to Pb at the time of crystallization and given a value according to the Stacey and Kramers (1975) bulk Earth evolution model at 42 Ma. More optimal methods of Pb_c correction have been discussed elsewhere (Chamberlain and Bowring, 2000; Schoene and Bowring, 2006; Schoene and Bowring, 2007), and include 1) acid leaching low-U domains from cogenetic phases such as K-feldspar (Housh and Bowring, 1991) and 2) isochron methods to determine initial Pb composition (Ludwig, 1998). Option (1) is not possible in these rocks because all samples except AD12 do not contain sufficient K-feldspar (and AD12 is relatively insensitive to Pb_c composition). Option (2) was attempted for all samples but failed in that MSWDs of both 2-D and 3-D regressions were >15, indicating that titanite from a given sample either are not the same age and/or do not have the same initial Pb composition. The former is likely the case. As such, a sensitivity test was carried out by varying the Stacey and Kramers (1975) model age between 0 and 200 Ma to explore the effect on calculated dates. Two important conclusions were reached: 1) that these titanite are sufficiently low in Pb* to be sensitive

to Pb_c composition and changing the model age from 42 Ma to 200 Ma raises the $^{206}Pb/^{238}U$ date between 50 and 200 ka. This distinction is often beyond the quoted uncertainty and therefore affects the interpreted cooling history of the samples, which is discussed in the main text.

SOM.2.2 Trace element and Hf isotope analysis

Zircon and titanite washes were recovered, aliquoted in two and analyzed separately for trace elements and Hf isotopes (for zircon), allowing us to correlate the U-Pb date to both trace element and Hf isotope signatures for the exact same volume of analyzed mineral. Trace element analysis methodology (U-Pb TIMS-TEA) is outlined in detail in Schoene et al. (2010b). Trace elements were also measured for dissolved titanite by the same method. Due to time constraints and the preliminary nature of this work, the same routine and sets of trace elements were measured for titanite as were for zircon, despite the abundance of other measurable trace elements in titanite. For this reason, we cannot normalize to any stoichiometric element, so absolute concentrations are unknown and trace elements are left as ratios.

The Hf fraction was measured at ETH Zürich in static mode on a NuPlasma™ multi-collector ICP-MS using an Aridus nebulizer for sample introduction. $^{176}Lu/^{177}Hf$ ratios of analyzed zircons were not determined but $^{176}Hf/^{177}Hf$ ratios were age corrected for a typical value of $^{176}Lu/^{177}Hf$ in zircon of 0.0005. The ^{176}Lu decay constant of (Scherer et al., 2001) was used for calculation; the correction stayed within limits of analytical precision of the measured $^{176}Hf/^{177}Hf$ ratios in all cases. The Hf isotopic ratios were corrected for mass fractionation using a $^{179}Hf/^{177}Hf$ value of 0.7325 and normalized to

$^{176}Hf/^{177}Hf = 0.282160$ of the JMC-475 standard (Blichert-Toft et al., 1997). The JMC-475 standard was measured every third position in similar measurement conditions as the zircon samples and yielded values between $^{176}Hf/^{177}Hf = 0.282130$ to 0.282190 according to the daily instrument tuning, both for batches doped with Yb as well as for non-doped batches. ^{176}Lu and ^{176}Yb present in analysis were corrected for using isotopic ratios for $^{176}Lu/^{175}Lu = 0.02656$ and $^{176}Yb/^{172}Yb = 0.586155$. Measured $^{176}Hf/^{177}Hf$ ratios typically have analytical errors of <0.5 ε units, though external 2σ reproducibility of standard measurements is ±0.5 ε units, which is used in data interpretations. $\varepsilon_{Hf(T)}$ values were calculated with $(^{176}Hf/^{177}Hf)_{CHUR(0)} = 0.282772$ (Bouvier et al., 2008) and 176Lu/177Hf = 0.0332.

REFERENCES CITED

Blichert-Toft, J., Chauvel, C., and Albarède, F., 1997, Separation of Hf and Lu for high-precision isotope analysis of rock samples by magnetic sector-multiple collector ICP-MS: Contributions to Mineralogy and Petrology, v. 127, p. 248-260.

Bouvier, A., Vervoort, J.D., and Patchett, P.J., 2008, The Lu-Hf and Sm-Nd isotopic composition of CHUR: Constraints from unequilibrated chondrites and implications for the bulk composition of terrestrial planets: Earth and Planetary Science Letters, v. 273, p. 48-57.

Chamberlain, K.R., and Bowring, S.A., 2000, Apatite-feldspar U-Pb thermochronometer: a reliable mid-range (~450˚C), diffusion controlled system: Chem. Geol., v. 172, p. 173-200.

Gerstenberger, H., and Haase, G., 1997, A highly effective emitter substance for mass spectrometric Pb isotope ratio determinations: Chemical Geology, v. 136, p. 309-312.

Griffin, W.L., Pearson, N.J., Belousova, E., Jackson, S.E., van Achterbergh, E., O'Reilly, S.Y., and Shee, S.R., 2000, The Hf isotope composition of cratonic mantle: LAM-MC-ICPMS analysis of zircon megacrysts in kimberlites: Geochimica et Cosmochimica Acta, v. 64, p. 133-147.

Griffin, W.L., Wang, X., Jackson, S.E., Pearson, N.J., O'Reilly, S.Y., Xu, X., and Zhou, X., 2002, Zircon chemistry and magma mixing, SE China: In-situ analysis of Hf isotopes, Tonglu and Pingtan igneous complexes: Lithos, v. 61, p. 237-269.

Hansmann, W., and Oberli, F., 1991, Zircon inheritance in an igneous rock suite from the southern Adamello batholith (Italian Alps): Contrib Mineral Petrol, v. 107, p. 501-518.

Housh, T., and Bowring, S.A., 1991, Lead isotopic heterogeneities within alkali feldspars: implications for the determination of initial lead isotopic compositions: Geochim. Cosmochim. Acta, v. 55, p. 2309-2316.

Krogh, T.E., 1973, A low contamination method for hydrothermal decomposition of zircon and extraction of U and Pb for isotopic age determination: Geochim. Cosmochim. Acta, v. 37, p. 485-494.

Ludwig, K.R., 1998, On the treatment of concordant uranium-lead ages: Geochim. Cosmochim. Acta, v. 62, p. 665-676.

Mattinson, J.M., 2005, Zircon U-Pb chemical-abrasion ("CA-TIMS") method: combined annealing and multi-step dissolution analysis for improved precision and accuracy of zircon ages: Chem. Geol., v. 220, p. 47-56.

Nowell, G.M., Kempton, P.D., Noble, S.R., Fitton, J.G., Saunders, A.D., Mahoney, J.J., and Taylor, R.N., 1998, High precision Hf isotope measurements of MORB and OIB by thermal ionisation mass spectrometry: insights into the depleted mantle: Chemical Geology, v. 149, p. 211-233.

Scherer, E., Münker, C., and Mezger, K., 2001, Calibration of the Lutetium-Hafnium clock: Science, v. 293, p. 683-687.

Schoene, B., and Bowring, S.A., 2006, U-Pb systematics of the McClure Mountain syenite: thermochronological constraints on the age of the 40Ar/39Ar standard MMhb: Contrib. Miner. Petrol., v. 151, p. 615-630.

Schoene, B., Crowley, J.L., Condon, D.C., Schmitz, M.D., and Bowring, S.A., 2006, Reassessing the uranium decay constants for geochronology using ID-TIMS U-Pb data: Geochim. Cosmochim. Acta, v. 70, p. 426-445.

Schoene, B., and Bowring, S.A., 2007, Determining accurate temperature-time paths in U-Pb thermochronology: an example from the SE Kaapvaal craton, southern Africa: Geochim. Cosmochim. Acta, v. 71, p. 165-185.

Schoene, B., Guex, J., Bartolini, A., Schaltegger, U., and Blackburn, T.J., 2010a, Correlating the end-Triassic mass extinction and flood basalt volcanism at the 100,000-year level: Geology, v. 38, p. 387-390. DOI: 10.1130/G30683.1.

Schoene, B., Latkoczy, C., Schaltegger, U., and Günther, D., 2010b, A new method integrating high-precision U-Pb geochronology with trace element analysis (U-Pb TIMS-TEA): Geochim. Cosmochim. Acta, v. 74, p. 7144-7159l doi:10.1016/j.gca.2010.09.016.

Stacey, J.C., and Kramers, J.D., 1975, Approximation of terrestrial lead isotope evolution by a two-stage model: Earth Planet. Sci. Lett., v. 26, p. 207-221.

Wasserburg, G.J., Jacobsen, S.B., DePaolo, D.J., McCulloch, M.T., and Wen, T., 1981, Precise determinations of Sm/Nd ratios, Sm and Nd isotopic abundances in standard solutions: Geochim. Cosmochim. Acta, v. 45, p. 2311-2323

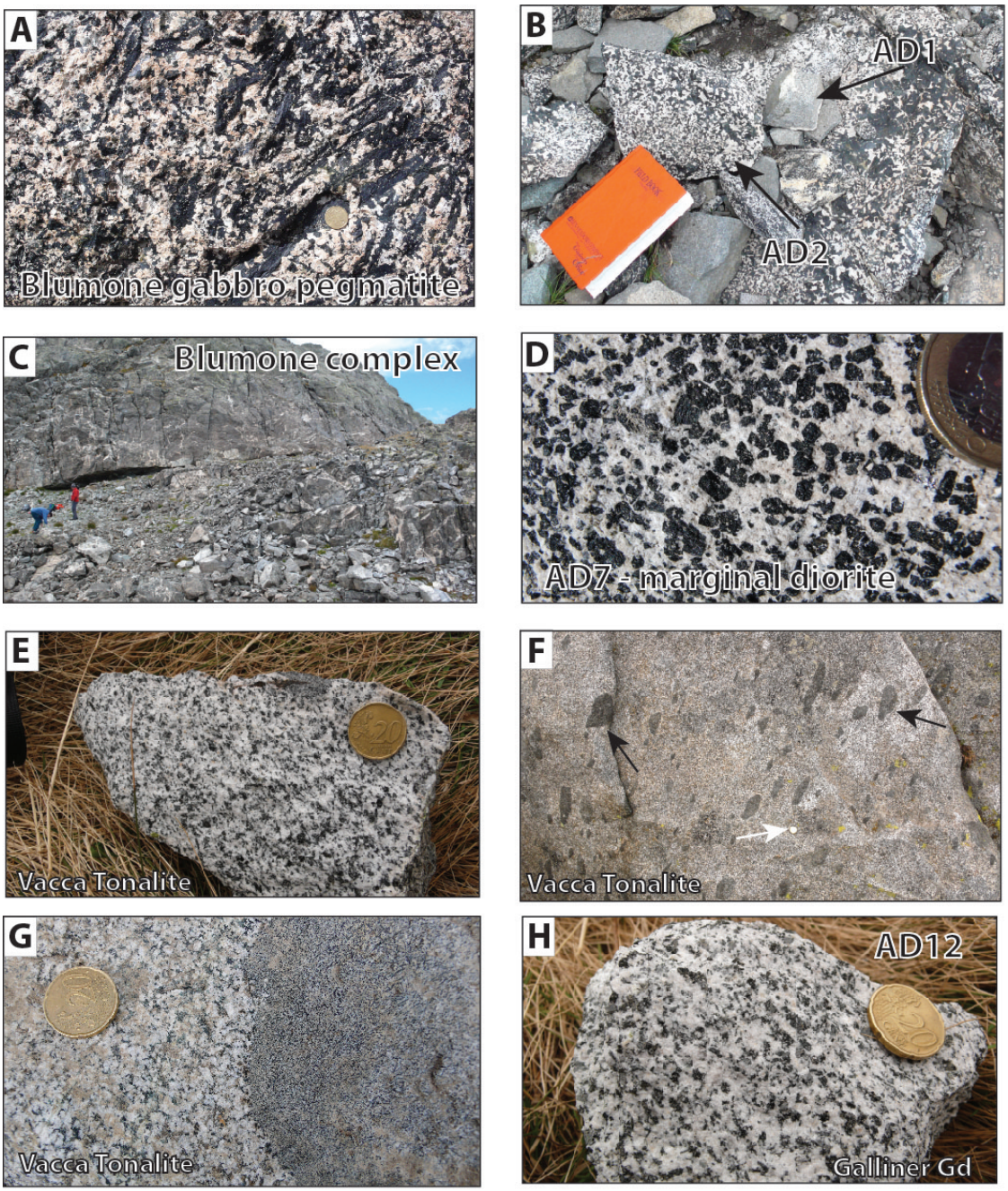

Fig SOM.1: Field and hand sample photos. (A) Typical Blumone gabbroic pegmatite. (B) fine-grained (AD1) and coarse grained (AD2) Blumone pegmatites. (C) outrcrop of Blumone complex. (D) hand sample of hornblende quartz diorite (AD7). (E) Typical Vacca tonalite with magmatic fabric defined by biotite and hornblende. (F) Typical Vacca tonalite with mafic enclaves (black arrows). White arrow = coin for scale. (G) example of mafic enclave included within the Vacca tonalite. (H) hand sample of Galliner granodiorite (AD12).

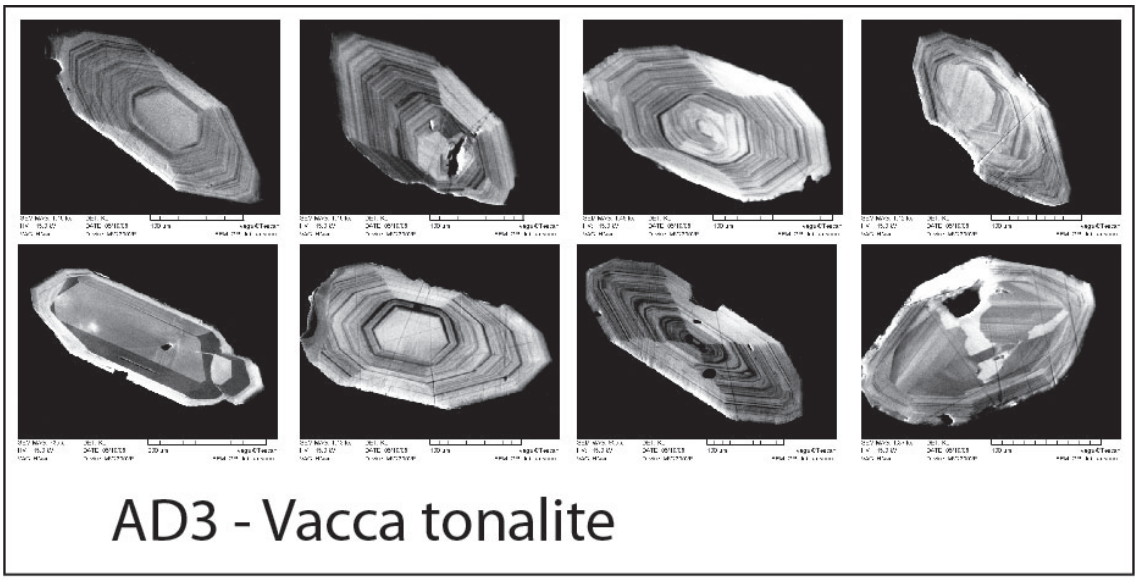

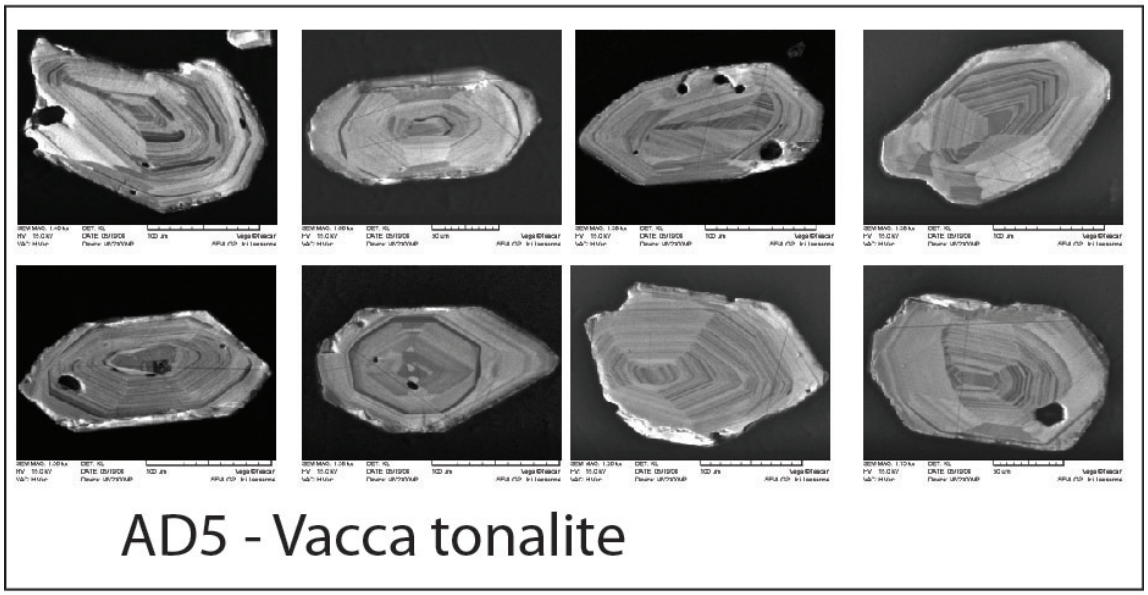

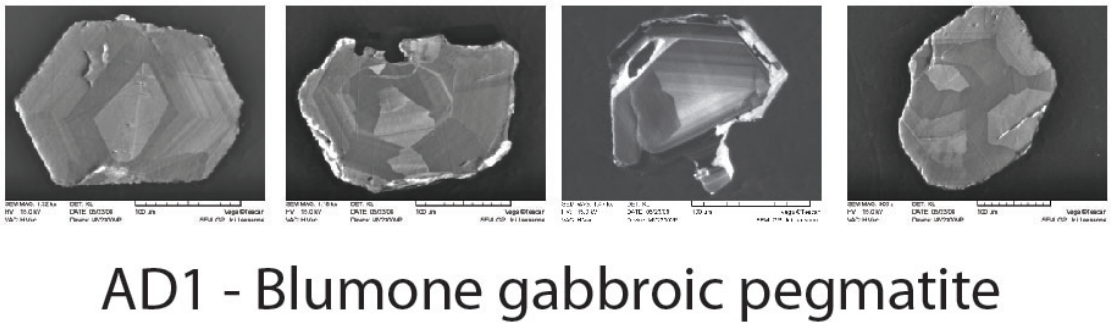

Fig. SOM2A: cathodoluminescence images of zircons from this study

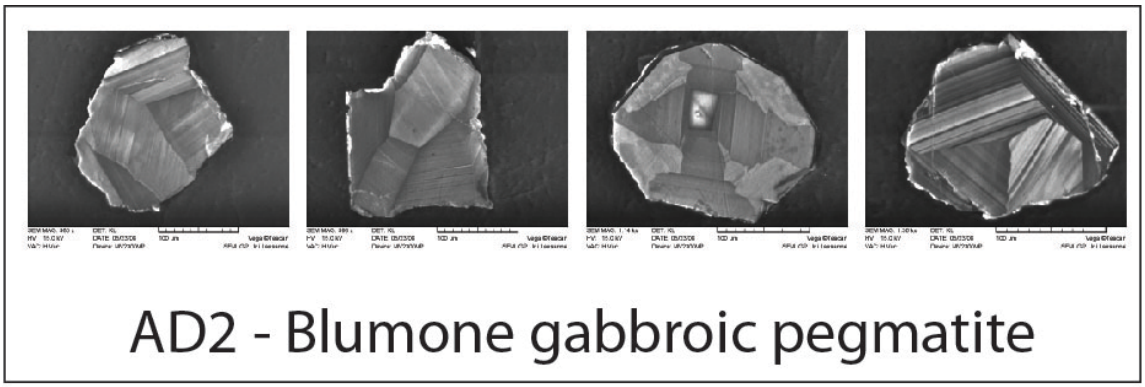

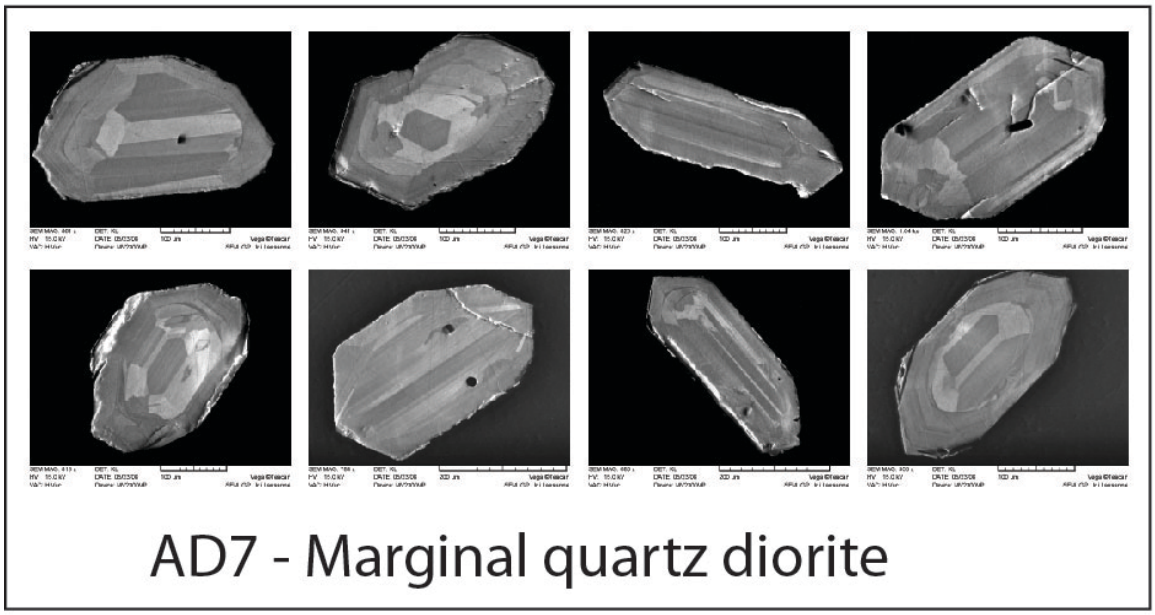

Fig. SOM2B: cathodoluminescence images of zircons from this study